DEVELOPMENT OF THE HELIUM-JET FED ON-LINE MASS SEPARATOR RAMA AND ITS APPLICATION TO STUDIES OF $T_z = -2$ NUCLEI

Table of Contents

DEVELOPMENT OF THE HELIUM-JET FED ON-LINE MASS SEPARATOR RAMA AND ITS APPLICATION TO STUDIES OF T_z = -2 NUCLEI

Dennis Michael Moltz

Department of Chemistry and
Lawrence Berkeley Laboratory
University of California
Berkeley, CA 94720

ABSTRACT

The study of nuclei far from beta stability is hampered greatly when the nuclide of interest decays in a manner identical to that of a nuclide produced in greater yield in the same bombardment. Attempts to observe the protons associated with the decay of the A = 4n, T_z = -2 series of beta-delayed proton emitters failed because of the large number of protons arising from the strong beta-delayed proton decay of the A=4n+1, T_z = -3/2 nuclides. One solution to this problem is through the use of an on-line mass separator. Development of the Berkeley helium-jet fed on-line mass separator RAMA is discussed as applied to studies of the A=4n, T_z = -2 nuclides.

RAMA, an acronym for Recoil Atom Mass Analyzer, has typical efficiencies of 0.1% for ~75 elements with melting points $\leq 2000^{o}C$. This efficiency permits decay studies to be readily performed on nuclei with production cross sections $\geq$500 μb for γ-ray spectroscopy and $\geq$1 μb for discrete energy charged particle spectroscopy. The mass range on the normalized RAMA focal plane is ±10%. The quoted efficiency is for a mass resolution of M/ΔM ~300.

RAMA has been used to observe two members of the A=4n, $T_z = -2$ series of beta-delayed proton emitters, ^{20}Mg and ^{24}Si. Observation of beta-delayed protons from a mass-separated sample of $^{20}Mg(t_{1/2}\sim95$ ms) establishes the mass-excess of the lowest T=2 (0^+) state in ^{20}Na (13.42±.05 MeV), thereby completing the mass twenty isospin quintet. A similar measurement of the decay of ^{24}Si ($t_{1/2}\sim100$ ms) establishes the mass-excess of the lowest T=2 (0^+) state in ^{24}Al (5.903±0.009 MeV). The mass 24 isospin quintet is incomplete because the mass of ^{24}Si remains unknown. In both cases, excellent agreement is obtained using only the quadratic form of the isobaric multiplet mass equation (IMME).

I. Introduction

Decay studies of both neutron deficient and neutron rich nuclei become increasingly difficult the further one explores from the line of β-stability. Conventional experimental techniques often are inadequate because competing reactions create a formidable background interfering with the study of nuclei with low production cross sections. Ideally, one would like to develop a technique which would yield a sample with a unique A and Z. Z identification has long been accomplished by chemical separations, but even with the advent of some fast chemistry techniques (Ko 74 and Ba 76) activities with half-lives below 1 s still remain essentially impossible to study. Chemical techniques yield no mass identification, however, leading to experimental designs which establish parent-daughter relationships in which the daughter has been previously characterized. Most compound nuclear reactions produce many isobars simultaneously, making mass separation (A identification) necessary.

Since most of the undiscovered nuclides are expected to have half-lives too short for off-line techniques, on-line mass analysis is a highly suitable approach for studying their decays. Many ingenious approaches to the development of such techniques have been tried. Isotope separator on-line (ISOL) systems have been developed to utilize many different accelerators and reactors. ISOL systems coupled to nuclear reactors generally rely on neutron induced fission of uranium (Zi 79 and Wo 77a). The uranium is contained in a graphite matrix maintained at ~2000°C which causes the more volatile fission products to diffuse from the matrix into the ion source for extraction

and subsequent mass analysis. Another approach has been the utilization of the large cross sections available in high energy proton induced spallation reactions. For example, the ISOLDE group at CERN develops only chemically selective ion sources to separate the products of interest from the many other elements which might be observed for a given isobar. Intense sources of radioactive beams are often produced of unique Z and A. Some types of elements studied to date include the rare gases (Ha 77a), the alkali metals (Ha 77c), and more recently ytterbium isotopes (De 79). The GSI on-line separator at the UNILAC uses very heavy ion induced reactions to produce very neutron deficient nuclei (Ki 77 and Ro 77a). The integrated target-ion source is highly efficient (10-15%) for more volatile elements with half-lives exceeding 1 s. These techniques have been primarily applied to studies of neutron-deficient nuclei in the trans-tin region. A similar ISOL system is employed at UNISOR (Sp 77) where studies have concentrated on Xe, I, Bi, Pb, Tl, and Hg isotopes.

Two other techniques for mass separation r identification have also been developed which are also generally chemically unselective. One system used extensively by Robertson (Ro 77b) uses time-of-flight mass identification following decay by either neutron, proton, or alpha emission. The mass resolution for this technique is very good, but no physical separation is obtained. Moreover, it is limited to either beta-delayed particle decays, direct particle emission, or alpha emission. The second technique, which is used at the BEMS-2 on-line separator at the JINR cyclotron (Ka 74), utilizes a gas jet to transport the activity to a catcher foil. The activity then diffuses

through the catcher foil which is maintained at very high temperatures (2500-3000^{o}C) where it undergoes surface ionizsation and subsequent acceleration into the mass separator.

We were interested in developing a general experimental system capable of mass analysis of radioactive species with half-lives as short as 50 ms and with simple application to a vast majority of the chemical elements. Experiments of immediate interest were study of the decay of the A = 4n, T_z = -2, series of nuclei; in general, these nuclei decay via β-delayed proton emission permitting accurate measurement of the lowest T = 2 state in the T_z = -1 member of an isospin quintet. Complete isospin quintets would allow further testing of the isobaric multiplet mass equation (IMME) first proposed by Wigner (Wi 57) and tested extensively in isobaric quartets (Be 79). If the production cross sections for these T_z = -2 nuclei are high enough, further information could be gained about the absolute log ft values associated with the $0^+ \rightarrow 0^+$ pure Fermi decay to the isobaric analog state of the daughter. An early attempt by our group to observe the decay of the A = 4n, T_z = -2, nuclide ^{40}Ti resulted in a beta-delayed proton spectrum dominated by decays associated with the well-known ^{41}Ti and ^{37}Ca nuclides copiously produced in competing reactions (Se 74). Clearly, mass separation is a necessity if the decays of nuclei such as ^{40}Ti are to be observed.

Another area of interest is the study of nuclei near the Z=50 closed shell. These nuclei exhibit beta-delayed particle emission and alpha-particle decay in addition to standard β-γ decay. Work in this region can be done by difficult γ-X-ray coincidence experiments such

as in the observation of ^{106}Sn (Va 78 and Bu 75). Clearly mass analysis would simplify the experiments substantially.

The study of light beta emitters provides another area where mass separation would prove invaluable. The observation and characterization of the half-lives and β-endpoints of interesting nuclei such as ^{21}O, ^{22}O, ^{19}N, ^{27}P, ^{31}Cl, and others in this region are of much current interest. Since these beta measurements are accomplished by decomposing the beta continuum (which in general does not correspond to decay to a single state in the daughter), and without mass separation, such a decomposition would be essentially impossible.

This brief introduction by no means exhausts the possibility of interesting experiments that can be performed with an ISOL system nor does it attempt to review the current status of the many existing and planned ISOL systems. An excellent review of experiments currently being pursued on ISOL systems is presented by Hansen (Ha 79). It is clear from this brief overview, however, that a chemically universal system would be the most useful to pursue to the types of experiments listed above. For this reason, we have developed the Berkeley on-line mass separator RAMA, an acronym for Recoil Atom Mass Analyzer. RAMA is shown schematically in Fig. 1-1. RAMA couples the elegant helium-jet recoil transport method (Ma 69a) with mass spectrometry techniques. The idea for such an ISOL system was originally proposed by Nitschke (Ni 70).

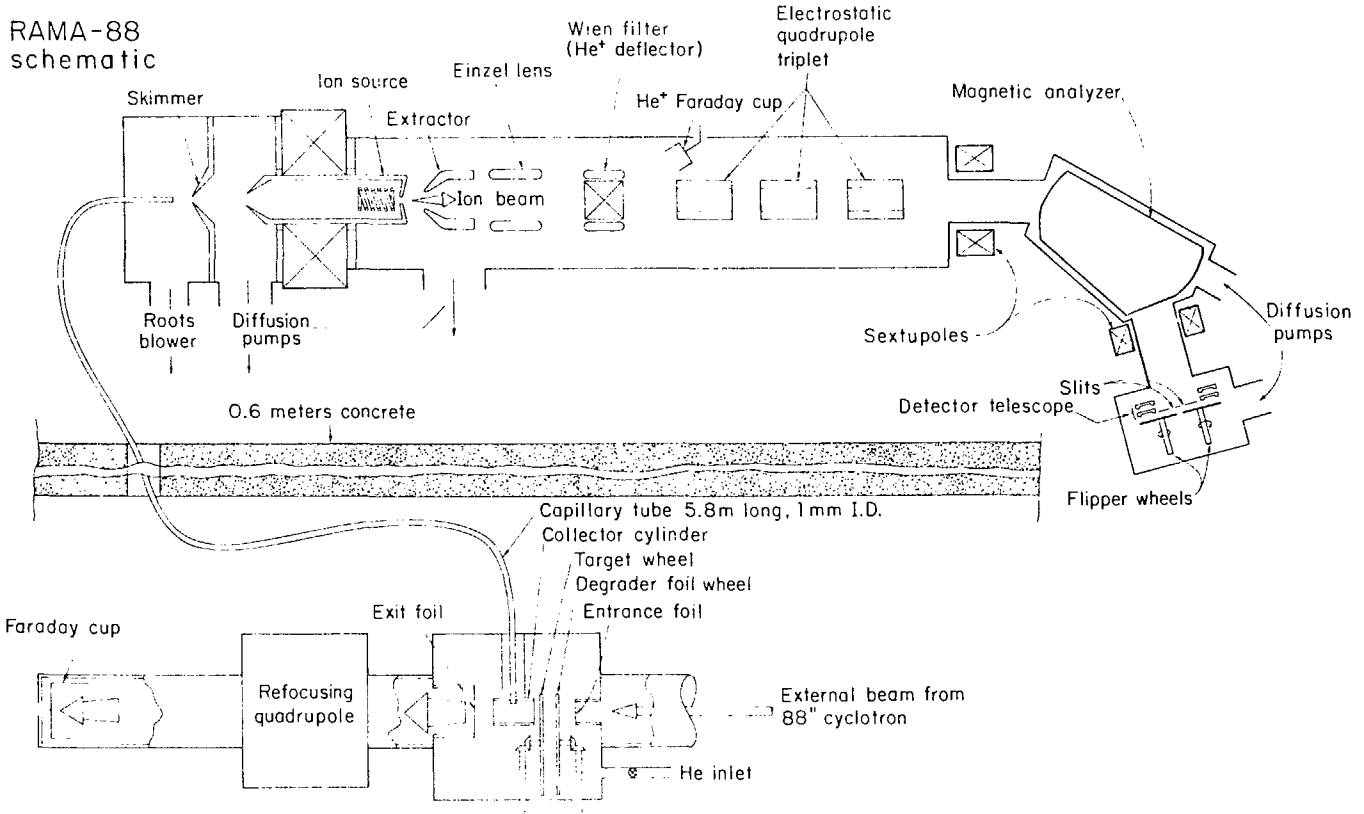

Fig. 1-1. Overall schematic diagram of RAMA.

II. Theory

This chapter will delve into three primary areas: a brief excursion into beta-delayed proton decay theory will be followed by two theoretical justifications for studying the A=4n, $T_z = -2$ nuclei. The latter will consist of presentations of the isobaric multiplet mass equation (IMME) and properties of the $0^+ \rightarrow 0^+$ pure Fermi beta transitions generally observed in the ground state decay of the A=4n, $T_z = -2$ nuclei.

A. Beta-delayed proton decay

Beta-delayed proton decay consists of two sequential yet distinct decay processes; these are beta decay to the emitter followed by proton decay to the daughter. Figure 2-1 shows the beta-delayed proton decay of a 0^+, (T=2) ground state as a subset of allowed beta decays. The selection rules for allowed decays predict that the decay from a (J^{π},T) state to a $(J'^{\pi'}, T')$ state occurs only when $|J-J'| \leq 1, \Delta\pi = \text{no}$, and $|T-T'| \leq 1$. Proton decay to the ground state of daughter from the isobaric analog state shown in Fig. 2-1 $((J^{\pi},T)\ (J'^{\pi'}, T'))$ is isospin forbidden. Measurements of these decay probabilities relative to isospin allowed decays provide a convenient test of the isospin purity of the isobaric analog state. Beta decay and proton decay will be discussed in general terms and in their relation to the A=4n, $T_z = -2$ series of beta-delayed proton emitters.

1) β-decay theory

Nuclear beta-decay is but one manifestation of what is assumed to be a universal weak interaction involving all elementary particles. It must also be assumed that the weak interaction stems from the

interaction of hadronic and leptonic currents. The weak interaction may well be mediated by a heavy vector boson in the same manner in which the photon mediates electromagnetic currents. Even though such an intermediate vector boson has not been observed, its postulation is essential to clarify the properties of the weak interaction.

It is best to begin by writing a weak interaction Lagrangian density between the appropriate currents and the vector boson as (Bl 69)

$$\mathcal{L}_{weak}(x) = g_1 J_\lambda(x) W_\lambda(x) + g_2 \ell_\lambda(x) W_\lambda(x) + \text{h.c. (hermitian conjugate)} \qquad (2\text{-}1)$$

where g_1 and g_2 are coupling constants; $J_\lambda(x)$ and $\ell_\lambda(x)$ are the hadronic and leptonic currents respectively; $W_\lambda(x)$ is the field operator for the intermediate vector boson; $x = (x_1, x_2, x_3, x_4 \equiv x, y, z, ict)$; λ is a space-time index ranging in value from 1,...4. The hadronic current may be further decomposed into strangeness conserving and non-conserving components, thus

$$J_\lambda = a J_\lambda^{\Delta S=0} + b J_\lambda^{\Delta S\neq 0} \; . \qquad (2\text{-}2)$$

$J_\lambda^{\Delta S=0}$ and $J_\lambda^{\Delta S\neq 0}$ may also be written as an octet representation of SU_3 (Sc 66 and Ge 64). Under these conditions, $J_\lambda^{\Delta S = 0}$ transforms as a vector and $J_\lambda^{\Delta S=1}$ ($J_\lambda^{\Delta S\neq 0} = J_\lambda^{\Delta S=1}$ since no $\Delta S=2$ decays have been observed) as a spinor in isospin space. Furthermore, these currents have a polar vector and an axial vector character. $J_\lambda^{\Delta S=0}$ can thus be written as

$$J_\lambda^{\Delta S=0} = V_\lambda + A \tag{2-3}$$

where V_λ is a polar vector operator and A_λ is an axial vector operator. No further details of these currents will be given here, but these rudiments are necessary to create a foundation for future discussions.

Finally, we consider the current operator ℓ_λ. This operator refers only to leptons (which do not experience the strong interaction) and thus, can be expressed in terms of field operators for the electron (e) and the muon (μ) and their corresponding neutrinos (ν_e, ν_μ). It should be noted that $\ell_\lambda(x)$ can be rewritten as

$$\ell_\lambda(x) = \ell_\lambda^e(x) + \ell_\lambda^\mu(x) \tag{2-4}$$

which insures the experimentally observed separate conservation of electron- and muon-type leptons. The beta-decay interaction stems from the interaction of this current with $J_\lambda^{\Delta S=0}$, which in the approximation of large mass (m_w) for the intermediate vector boson (Le 60 and Ch 61), yields the following form for the effective β-decay Lagrangian density,

$$L_\beta(x) = \frac{g_1 g_2}{(m_w)^2} (J_\lambda^{\Delta S=0}(x)\ell_\lambda^*(x) + \text{h.c.}) \quad . \tag{2-5}$$

The operator $\ell_\lambda^*(x)$ is related to the Hermitian conjugate operator ℓ_λ^+ by

$$\ell_\lambda^* = n_\lambda \ell_\lambda^+ \tag{2-6}$$

where $n_\lambda = 1$ for $\lambda = 1,2,3$ and $n_4 = -1$. In a similar manner the Lagrangians responsible for muon decay and strangeness changing leptonic decays are given by

$$L_\mu(x) = \left(\frac{g_2}{m_w}\right)^2 (\ell_\lambda^\mu \ell_\lambda^{e*}(x) + \text{h.c.}) \tag{2-7}$$

and

$$L_S(x) = \frac{g_1' g_2}{(m_w)^2} (J_\lambda^{\Delta S=1}(x)\, \ell_\lambda^*(x) + \text{h.c.}). \tag{2-8}$$

Redefining the coupling constants to eliminate the dependence on the mediation of these currents by a vector boson, we obtain

$$\frac{g_1 g_2}{(m_w^2)} = \frac{1}{\sqrt{2}} G \cos \theta_c = \frac{1}{\sqrt{2}} G_\beta \tag{2.9a}$$

$$\left(\frac{g_2}{m_w}\right)^2 = \frac{1}{\sqrt{2}} G_\mu \tag{2-9b}$$

$$\frac{g_1' g_2}{(m_w)^2} = \frac{1}{\sqrt{2}} G \sin \theta_c \tag{2-9c}$$

where θ_c is known as the Cabbibo angle which will be discussed in more detail later.

Initially we consider the beta-decay of a free nucleon (in reality only the decay $n \rightarrow p + e^- + \bar{\nu}_e$ is energentically allowed) whose transition matrix element is given by

$$M_{\beta^-} = \langle\, pe^-\bar{\nu}_e \left| \int L_\beta(x) d^4x \right| n \,\rangle \tag{2-10}$$

which in consideration of equation (2-3) can be rewritten as

$$M_{\beta^-} = - \frac{1}{\sqrt{2}}\, i\, G_\beta \langle\, p | V_\lambda + A_\lambda | n \,\rangle\, Z(e,\bar{\nu}) \delta(p+e+\bar{\nu}+n) \tag{2-11}$$

where $p,e,\bar{\nu},n$ are the four momenta for the particles indicated and $\delta(p + e + \bar{\nu} + n)$ represents conservation of momentum. If we assume plane wave spinor functions for the electron and the neutrino (Bl 69), M_{β^-} can also be expressed in terms of a beta decay Hamiltonian as

$$H_{\beta^-}(r) = \frac{1}{\sqrt{2}}\, G_\beta \left[i g_V L_4(r) - g_A \sigma \cdot \underline{L}(\underline{r}) \right] \tag{2-12}$$

where L represents the contributions from the electron and neutrino wave functions and σ is the Pauli spin operator. By redefining the coupling constants such that $G_V = g_V G_\beta$ and $G_A = -g_A G_\beta$ the usual polar and axial vector coupling constants, respectively, and by replacing specific neutron and proton wave functions with an isospin formulation, the beta decay Hamiltonian for both negatron and positron emission can be written as

$$H_{\beta^-}(r) = \frac{1}{\sqrt{2}} [iG_V L_4(r) + G_A \sigma \cdot \underline{L}(r)] \tau_- \qquad (2\text{-}13a)$$

$$H_{\beta^+}(r) = \frac{1}{\sqrt{2}} [iG_V L_4^*(r) + G_A \sigma \cdot \underline{L}^*(r)] \tau_+ \qquad (2\text{-}13b)$$

where $\tau_\pm$ are isospin raising and lowering operators given by

$$\tau_\pm = \tau_x \pm i\tau_y \text{ and } \tau_z|n\rangle = \frac{1}{2}, \ \tau_z|p\rangle = -\frac{1}{2} \text{ for } |n\rangle \text{ and } |p\rangle$$

neutron and proton states, respectively. Since β-decay generally occurs in more complex systems, this Hamiltonian must be generalized to the many-body case as

$$H_{\beta^-} = \frac{1}{\sqrt{2}} \sum_{i=1}^{A} [iG_V L_4(r_i) + G_A \sigma^{(i)} \cdot \underline{L}(r_i)] \tau_-^{(i)} \qquad (2\text{-}14)$$

A similar result is obtained for positron decay.

This basis thus allows us to consider the β^--decay transition between two nuclear states $|i\rangle$ and $|f\rangle$. The relevant matrix element M_{β^-} is given by

$$M_{\beta^-} = \langle f|H_{\beta^-}|i\rangle \qquad (2\text{-}15)$$

where H_{β^-} is given in equation (2-14). By a standard application of perturbation theory, an expression for the half-life (t) of an allowed beta-transition is obtained (Bl 66),

$$\underline{ft} = \frac{c}{G_V^2 |M_V|^2 + G_A^2 |M_A|^2} \qquad (2\text{-}16)$$

where $\underline{f}$ is known as the statistical rate function. $\underline{f}$ depends upon the charge Z of the decaying nucleus and the beta-endpoint energy (E_o) and is given by the integral

$$\underline{f}\,(Z,E_o) = \int_1^{E_o} pE\,(E_o-E)^2\,F(Z,E)\,dE \qquad (2\text{-}17)$$

where F(Z,E) depends on the solutions of the Dirac equation for the emitted electron. The maxtrix elements M_A and M_V are given for generalized beta-decay by

$$M_A = \langle f|\sum_i \tau_{\pm}^{(i)}\sigma^{(i)}|i\rangle \qquad (2\text{-}18)$$

and

$$M_V = \langle f|\sum_i \tau_{\pm}^{(i)}|i\rangle \quad . \qquad (2\text{-}19)$$

M_A is known as the Gamow-Teller or axial vector matrix element while M_V is known as the Fermi or vector matrix element. In the case of pure isospin states, M_V may be evaluated as

$$M_V = \langle T,T_z\pm 1|T_{\pm}|T,T_z\rangle = [(T\mp T_z)(T\pm T_z+1)]^{1/2} \quad . \qquad (2\text{-}20)$$

For impure isospin states where a^2 represents the isospin purity of a state mixed with a second state of T' = T 1, M_V^2 is given by

$$M_V^2 = [T(T+1) - T_{z_i}T_{z_f}]\,a^2 \quad . \qquad (2\text{-}21)$$

These results when considered together with the spatial transformation properties of the two operators yield the known Fermi selection rules of $\Delta J = 0$, $\Delta\pi$ = no and the Gamow-Teller selection rules of $|\Delta J| \leq 1$ $(0 \not\rightarrow 0)$, $\Delta\pi$ = no for allowed transitions. Forbidden transitions are not relevant to further discussion, but are covered in detail by Konopinski and Rose (Ko 65). Both allowed and forbidden transitions may be classified according to their comparative half-lives or log ft's (see equation (2-16)) (Ra 73). Of particular interest are the $J^{\pi}=0$, $\Delta\pi$ = no, $\Delta T = 0$ or superallowed transitions between members of an isospin multiplet. The special case of $0^+ \rightarrow 0^+$ decay where $M_A \rightarrow 0$ is of particular interest and will be considered in greater detail in Section C.

2). Proton emission from unbound levels

Proton emission from unbound levels is more clearly illustrated by the generalized decay scheme for a member of the A=4n, T_z=-2 series of beta delayed proton emitters shown in Fig. 2-1. The A(Z+2) ground state undergoes beta-decay to many states in the daughter, including superallowed decay to the 0^+(T=2) excited state. This state may then either γ-decay or emit a proton with energy commensurate with the mass of the A-1(Z) nucleus (for decay to the ground state). Proton decay to the ground state is generally isospin forbidden, and thus, a small amount of isospin mixing is assumed from nearby 0^+ states. The ground state of the A(Z+1) nucleus may also beta-decay to states of the A(Z) nucleus, but direct proton decay to the A-1(Z-1) nucleus from these states is generally energetically impossible.

The probability for proton emission may be simply examined by considering the transmission coefficient T for a proton of energy E and angular momentum ℓ(Ma 69b)

$$T = \exp\left(-\frac{2}{\hbar}\int[2m\,(V(r)-E)]^{1/2}\,dr\right) . \qquad (2\text{-}22)$$

The potential V(r) is often represented by the simple potential

$$V(r) = V_c(r) + V_\ell(r) = \frac{z_1 z_2 e^2}{r} + \frac{\ell(\ell+1)\hbar^2}{2mr^2} \qquad (2\text{-}23)$$

where $V_c(r)$ and $V_\ell(r)$ are the Coulomb and centrifugal barriers, respectively. For the special case of an ℓ=0 proton, V(r) becomes

$$V(r) = \frac{Ze^2}{r} \qquad (2\text{-}24)$$

Substituting this potential into (2-22) and evaluating at the appropriate limits, we obtain

$$T = \exp\left(\frac{-8Ze^2mb}{\hbar^2}\right)\left[\cos^{-1}\left(\frac{R}{b}\right)^{1/2} - \left(\frac{R}{b} - \frac{R^2}{b^2}\right)^{1/2}\right] \qquad (2\text{-}25)$$

where $b = \frac{Ze}{E}$ and $R = r_o\,(1 + A^{1/3})$. This formula yields proton decay lifetimes of $\sim 10^{-18}$ sec for ~3 MeV proton when $A \approx 36$.

Similar results may also be obtained by considering the proton partial decay width Γ_p as a function of the proton penetrability P_ℓ and the proton reduced width γ_p^2. These are related by (Ha 74)

$$\Gamma_p = 2P_\ell \gamma_p^2 \tag{2-26}$$

where P_ℓ is dependent upon both the Coulomb and centrifugal potential barrier (see (2-23)) and ℓ is the angular momentum of the emitted proton and is frequently consistent with the lowest value of $|J_i - J_f|_{min}$ which also obeys $\Delta\pi = (-1)^\ell$. The advantage of this approach is that P_ℓ may be calculated from the time reversed action,

$$p + A\text{-}1(Z) \rightarrow A(Z+1), \tag{2-27}$$

where the well known regular and irregular Coulomb wave functions, F_ℓ and G_ℓ, may be utilized, These wave functions represent solutions to the Schrodinger equation for a Coulomb potential which yields

$$P_\ell = \frac{kR}{F_\ell^2 + G_\ell^2} \tag{2-28}$$

where k is the wave number of the incident proton which is given by the deBroglie relationship,

$$k = \frac{1}{\lambda\!\!\!^{-}} = \frac{p}{\hbar} = \frac{(2\mu E)^{1/2}}{\hbar} = 0.2187\ (\mu E)^{1/2}\ \text{fm}^{-1} \tag{2-29}$$

where μ is the reduced mass in AMU and E is the center of-mass proton energy in MeV.

The primary disadvantage with equation (2-26) is in the calculation of γ_p^2 because of its dependence on a given nuclear model. This disadvantage becomes transparent when γ_p^2 is reduced to

$$\gamma_p^2 = \gamma_w^2 \theta_p^2 \qquad (2\text{-}30)$$

where θ_p^2 is the dimensionless reduced width whose estimates are nuclear model dependent. γ_w^2 is termed the Wigner sum-rule limit (La 58) and is given by (Ma 68)

$$\gamma_w^2 = \frac{3\hbar^2}{2\mu R^2} = \frac{62.70}{\mu R^2} \text{ (MeV)} \qquad (2\text{-}31)$$

and represents the maximum allowable reduced width. θ_p^2 represents the probability of finding a proton of a given nuclear configuration (e.g., appropriate nuclear shell) at the nuclear surface. It should also be noted that proton decay to excited states in the daughter may be treated in the same manner as decay to the ground state with further applications of equations (2-26) and (2-30).

B. Isobaric multiplet mass equation

Of particular emphasis in this research is the study of the A=4n, T_z = -2 series of beta-delayed proton emitters. A major experimental advantage arises in studying beta-delayed proton emission because the observation of discrete proton decay energies can easily be used to relate separation energies of various nuclear states between different nuclei, e.g., the separation energy between the mass of the ground state of the A-1(Z) nucleus and the 0^+(T=2) excited state in A(Z+1) nucleus in Fig. 2-1. The example just stated represents a method by which the lowest T=2 state in the T_z = -1 member of an A=4n isospin quintet may be studied. Experimentally the only roadblocks to completing an isospin quintet are often the measurement of the mass of

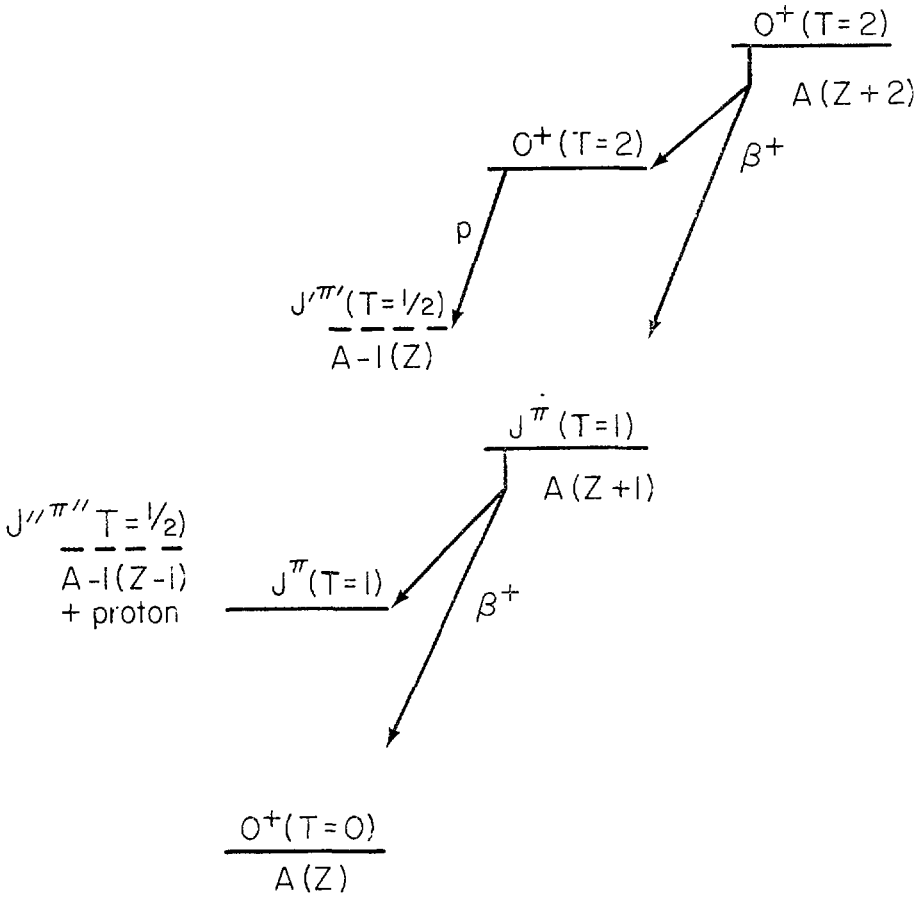

XBL 794-1101

Fig. 2-1. Generalized beta-delayed proton decay scheme of an $A = 4n$, $T_z = -2$ nucleus.

this state and the mass of the A(Z+2) ground state. Completion of a quintet would allow futher testing of the remarkably successful quadratic mass equation originally proposed by Wigner (Wi 57) relating the 2T+1 members of an isospin multiplet. This equation is known as the isobaric multiplet mass equation (IMME).

The isobaric multiplet mass equation may be written as

$$M(A,T,T_z) = a(A,T) + b(A,T)T_z + c(A,T)T_z^2 \qquad (2\text{-}32)$$

where T_z is the z-component of the isospin and is represented by

$$T_z = \frac{N-Z}{2} \qquad (2\text{-}33)$$

where N and Z are the number of neutrons and protons, respectively. In the absence of charge dependent interactions, the isospin T is a good quantum number and all the masses of an isospin multiplet are degenerate. The interactions between protons are, however, charge dependent and lead to an energy shift between members of an isospin multiplet and to isospin admixtures. This Coulomb interaction between the protons of a nucleus can be written as the sum of an isoscalar, an isovector, and an isotensor operator. This may be expressed as (Ja 63 and Be 79)

$$H_c = H_c^{(0)} + H_c^{(1)} + H_c^{(2)} \qquad (2\text{-}34)$$

First order perturbation theory permits us to calculate the major contribution ot the Coulomb energies of all of the members of an isospin multiplet.

In first order, the Coulomb energy is given by the expectation value of H_c for each member of the 2T+1 degenerate eigenstates $|\alpha TT_z\rangle$ of the charge independent part of the Hamiltonian written as

$$E_c(A,T,T_z) = \langle \alpha TT_z | H_c | \alpha TT_z \rangle$$

$$= \sum_{k=0}^{2} \langle \alpha TT_z | H_c^{(k)} | \alpha TT_z \rangle \qquad (2\text{-}35)$$

where α represents all of the quantum numbers necessary to specify the space-spin part of the nuclear wave function. By a standard application of the Wigner-Eckart theorem, the T_z dependence of the expectation values of H_c may be factored out as

$$M(A,T,T_z) = \sum_{k=0}^{2} (-1)^{T-T_z} \begin{pmatrix} T & k & T \\ -T_z & 0 & T_z \end{pmatrix} \langle \alpha T \| H_c^{(k)} \| \alpha T \rangle$$

$$= E_c(0)(A,T) - T_z E_c^{(1)}(A,T) \qquad (2\text{-}36)$$

$$+ (3T_z^2 - T(T+1))\, E_c^{(2)}(A,T)$$

with

$$E_c^{(0)}(A,T) = \langle \alpha T | H_c^{(0)} | \alpha T \rangle \qquad (2\text{-}37)$$

$$E_c^{(1)}(A,T) = -(T(T+1))^{-1/2} \langle \alpha T | H_c^{(1)} | \alpha T \rangle \qquad (2\text{-}38)$$

$$E_c^{(2)}(A,T) = (T(T+1)(2T-1)(2T+3))^{-1/2} \langle \alpha T | H_c^{(2)} | \alpha T \rangle \quad . \qquad (2\text{-}39)$$

Equation (2-36) is quadratic in T_z and equations (2-37)-(2-39) represent expressions for the scalar, vector, and tensor Coulomb energies, respectively. These Coulomb energies are dependent only upon A, T, and α, even though the explicit dependence on α is not shown.

The masses of the members of an isospin multiplet are given by

$$M(A,T,T_z) = 1/2(n+m_H)A + (m_n - m_H)\, T_z + \langle TT_z | H_o | TT_z \rangle + \langle TT_z | H_1 | TT_z \rangle + E_c(A,T,T_z) \quad . \qquad (2\text{-}40)$$

Upon substituting equation (2-36) for $E_c(A,T,T_z)$ and associating all coefficients of (T_z^0), (T_z^1), and (T_z^2), the standard IMME in equation (2-32) is obtained with

$$a(A,T) = 1/2(m_n+m_H)A + \langle TT_z | H_0 | TT_z \rangle + E_c^{(0)}(A,T) - T(T+1)E_c^{(2)}(A,T) \quad , \qquad (2\text{-}41)$$

$$b(A,T) = (m_n - m_H) - E_c^{(1)}(A,T) \qquad (2\text{-}42)$$

$$c(A,T) = 3E_c^{(2)}(A,T) \quad . \qquad (2\text{-}43)$$

The operator H_o is the charge independent part of the nuclear Hamiltonian and thus independent of T_z while other small charge dependent effects are contained within H_1 (e.g., electrostatic self-energy of the protons). These effects will not, however, change the quadratic T_z-dependence of the isobaric multiplet mass equation assuming they can be treated in first order perturbation theory and are tensors of rank two or less in isospin space.

These latter assumptions about the nature of H_1 may be experimentally checked. Second order perturbation theory generates terms $d(A,T)T_z^3$ and $e(A,T)T_z^4$ which can be important in general or in particular cases in which one of the states of an isospin multiplet is particle unstable or only weakly bound while the other states are bound; this latter situation arises for example in the mass nine (Na 75) quartet.

The wavefunctions for the various members of an isobaric multiplet should differ only by T_z (i.e., they are simply related by the operator T_- introduced in section A.). These wavefunctions may be changed greatly when nearby states with the same spin and parity, but with different isospin, mix with the state of interest. Some manifestations of isospin mixing for both isospin quartets and quintets is shown in Fig. 2-2. The dashed lines in Fig. 2-2 represent the unperturbed levels and the solid lines immediately above represent the isospin mixed state. In quartets, mixing in the $T_z=\pm 1/2$ nuclei primarily changes cT_z^2 while dT_z^3 remains small. In quintets, however, unique isospin mixing by T=0 states into the T=2 state in the $T_z=0$ member would make $eT_z^4 \neq 0$ (Be 79). Mixing of this T=0 state

with nearby T=1 states would change cT_z^2 and dT_z^3 and to a lesser extent, eT_z^4. Mixing in the $T_z=\pm 1$ nuclei gives similar results. It thus becomes imperative to locate the nearby T=0 state in the $T_z=0$ member of the isospin quintet determine the $\Delta T=2$ contribution to eT_z^4. To properly check for a nonzero quartic term requires completed quintets. The only completed quintet to date is mass eight (Be 79 and Ro 76), where ^8C is unbound to prompt nucleon emission; data on this quintet exhibit significant deviation from the quadratic IMME. Since the previously mentioned mass nine system is the only case in which deviation from the quadratic IMME has been observed out of twenty completed quartets, clearly more completed quintets are necessary to discover whether or not the mass eight system is indeed an anomaly. Completed quintets allow the unique determination of the coefficients a,b,c,d, and e of the perturbed IMME as a function of the experimental masses; these are shown in Fig. 2-3. The previous statement about the manifestation of isospin mixing in the $T_z=0$ member due to T=0 admixtures may be seen in the equations for d and e. Only by comparing the experimental results with theoretical coefficients in equation (2-32) can information about charge-dependent nuclear forces be obtained. This especially applies to second and higher order perturbations.

C. $0^+ \rightarrow 0^+$ pure Fermi transitions

As mentioned in section A, nuclear beta-decay arises from the interaction of the weak leptonic current and the strangeness conserving current $J_\lambda^{\Delta S=0}$ which by equation (2-3) could be decomposed into a polar and an axial vector. These two currents mediate the Fermi and

Gamow-Teller beta-decays, respectively. We will primarily confine ourselves to a discussion of the special case of the $0^+ \cdot 0^+$ pure Fermi transitions, however, a brief description of Gamow-Teller transitions is in order.

The matrix element for Gamow-Teller beta decay is given in equation (2-18). The operator $\sum_i \tau_+^{(i)} \sigma^{(i)}$ is equivalent to A_λ and arises from a description of partially conserved axial vector current theory (PCAC). Partial conservation (as opposed to full conservation) is necessitated by the experimental observation of pion decay. Total conservation would require a stable pion. A more complete description of PCAC may be found in de Shalit and Feshbach (De 74). One of the triumps of weak interaction theory is the prediction of the ratio of the coupling constants $G_A/G_V = -1.25$ (see equation (2-13)). This has been experimentally verified in the decay of the free neutron. Considerations of many different nuclear beta-decays have demonstrated a smaller effective value for G_A (than that derived from G_β). Wilkinson obtains a renormalized value of $(0.902 \pm 0.035)G_A$ for G_{Ae} (the effective axial vector coupling constant) (Wi 73b). An attempt has been made to explain this quenching effect (Bl 75), but no single mechanism satisfactorily explains all the observed changes in G_{Ae}. Further details about this renormalization of the axial vector coupling constant may be found elsewhere (Wi 74 and Bl 75).

It has been shown that $G = G_\mu$ ($G_V = G \cos \theta_c$ where θ_c is the Cabbibo angle) within experimental error bars. The value for G_μ has been determined from the decay of the muon

$$\mu^- \rightarrow e^- + \bar{\nu}_\mu + \nu_e \qquad (2\text{-}46)$$

as (Ha 75)

$$G_\mu = (1.43563 \pm 0.00022) \times 10^{-49} \text{ erg cm}^3 \quad . \qquad (2\text{-}47)$$

"When man discovers that two things between which he can see no obvious connection are in fact approximately equal, he usually assumes that nature must, for a private reason, have made them exactly equal. It is so long ago that we became used to the idea that the electric charges of the electron and proton are identical that we no longer marvel at it; the universality of electric charge has become a law of the nature, i.e., something that we cannot understand" (Wi 72b). The extension of this concept to the equality $G = G_\mu$ can only lead to the postulation of a conserved vector current (CVC), i.e., that

$$\frac{\partial V_\lambda}{\partial x_\lambda} = 0 \qquad (2\text{-}48)$$

where V_λ is the vector current part of $J^{\Delta S=0}$ and the x_λ are space-time operators. Equation (2-47) is in complete analogy with the situation in electromagnetic theory, in which the electric current operator is conserved and consequently the electromagnetic coupling constant is not renormalized by strong interactions.

One method to check CVC is by studying nuclear beta-decays in which the Gamow-Teller matrix element is identically zero. This reduces equation (2-16) to

$$\underline{ft} = \frac{C}{G_V^2 |M_V|^2} \quad . \tag{2-49}$$

Using equation (2-20) for pure isospin states to obtain a value for M_V and combining this with a measurement of the half-life for a pure Fermi transition would give a value for G_V. The only pure Fermi transitions are $0^{\pm} \rightarrow 0^{\pm}$ decays. CVC suggests that all $\underline{ft}$ values for decays with the same matrix element should have the same comparative half-life ($\underline{ft}$). Electromagnetic radiative corrections must, however, be included in the $\underline{ft}$ value before a comparison may be made. This modified $\underline{Ft}$ value must be used to determine a value for G_V.

To obtain this modified $\underline{Ft}$ value, we rewrite equation (2-49) (To 73) as

$$\underline{ft}\ (1+\delta_R) = \frac{C}{G_V^2 |M_V|^2} \tag{2-50}$$

$$\text{with } G_V'^2 = G_V^2\ (1+\Delta_R) \tag{2-51}$$

$$M_V'^2 = |M_V|^2\ (1-\delta_c) \tag{2-52}$$

where δ_R is termed the outer radiative correction, Δ_R is the inner radiative correction, and δ_c modifies the Fermi matrix element to include Coulomb and nuclear charge-dependent forces. By defining $\underline{Ft}$ as

$$\underline{Ft} \equiv \underline{ft}\ (1+\delta_R)\ (1-\delta_c). \tag{2-53}$$

we may simply relate this corrected value to G_V via

$$\underline{Ft} = \frac{c}{G_V^2 |M_V|^2 (1+\Delta_R)} \qquad (2\text{-}53)$$

The inner radiative correction Δ_R is not included in the definition of $\underline{Ft}$ since it represents the collection of nucleus independent terms whereas Δ_R and δ_c depend on the decaying nucleus (Ha 75).

These radiative corrections arise from the interaction of the decaying nucleon and the emitted positron with the external electromagnetic field. They may be expressed as a perturbation series in $Z\alpha$ ($\alpha=e^2/\hbar c$) (Be 69), where all terms $z^m\alpha^n$, $m\leq n$, are present. Much work has been done in calculating these corrections such as those of order $Z\alpha^2$ determined by Jaus and Rasche (Ja 70). Other terms are reviewed by Hardy and Towner (Ha 75). When all of these corrections are applied to sixteen different superallowed Fermi beta-decays between A=10 and A=54 (Ha 75) including both $T_z = -1$ and $T_z = 0$ nuclides as parents, a weighted $\overline{\underline{Ft}}$ value of 3081.7±1.9 s is obtained. All experimental data points are consistent with this value within the known error bars. Subsequent remeasurements for several of the higher mass nuclei from A=34 to A=50 (Wi 76) yield a weighted $\overline{\underline{Ft}}$ of 3084.5±1.9 s. Since all these results consist of decays of only $T_z = 0$ and $T_z = -1$ nuclei, clearly comparison with several $T_z = -2$ decays would be of great interest.

Careful measurements and calculations of these $\underline{Ft}$ values allow us to check various weak interaction models. Cabbibo universality gives

$$G_V = G \cos \theta_c = G_\mu \cos \theta_c \quad . \tag{2-54}$$

Recalling that

$$G_V = G_V' (1+\Delta_R)^{-1/2} \tag{2-55}$$

shows that a measurement of θ_c could yield information about Δ_R. The most natural source of the Cabbibo angle is hyperon beta-decay (Ro 74). When this value for θ_c is compared with other measurements, the nominal value

$$\sin \theta_c = 0.229 \pm 0.003 \text{ or } \theta_c = 0.231 \pm 0.003 \tag{2-56}$$

is obtained. This value for θ_c when taken together with the value for G_μ given in equation (2-47) yields a value of $(2.09 \pm 0.16)\%$ for Δ_R (Wi 76). Examination of Δ_R permits us to make certain comparisons and distinctions. This value for Δ_R sets limits on the mass of the intermediate vector boson (see section A) for different quark models (Ha 75). These limits are $20 \leq M_W \leq 35$ GeV for a model of four quarks of integral charge and $M_W > 80$ GeV for three colored quartets. If we assume the Weinberg-Salam model is correct (We 74) where $M_W > 74.6$ GeV, then a value for the mean charge of the quarks making up the nucleon may be obtained from Δ_R (Si 74). Combining this result with deep inelastic neutrino and electron scattering gives values for the effective charges of the "up" and "down" quarks of $Q_u = 0.67 \pm 0.05$ and $Q_d = -0.33 \pm 0.08$ (Wi 76). It should be noted

that incorporating Δ_R into other quark models gives results consistent with known experimental observations.

Measurements of $0^+ \rightarrow 0^+$ pure Fermi nuclear beta-decays provide a unique and elegant method for relating traditional low-energy nuclear physics with particle physics via further testing of conserved vector current theory. More precise determination of experimental half-lives and an expansion of the data base to include decays of $T_z = -2$ nuclei would clearly be of great utility.

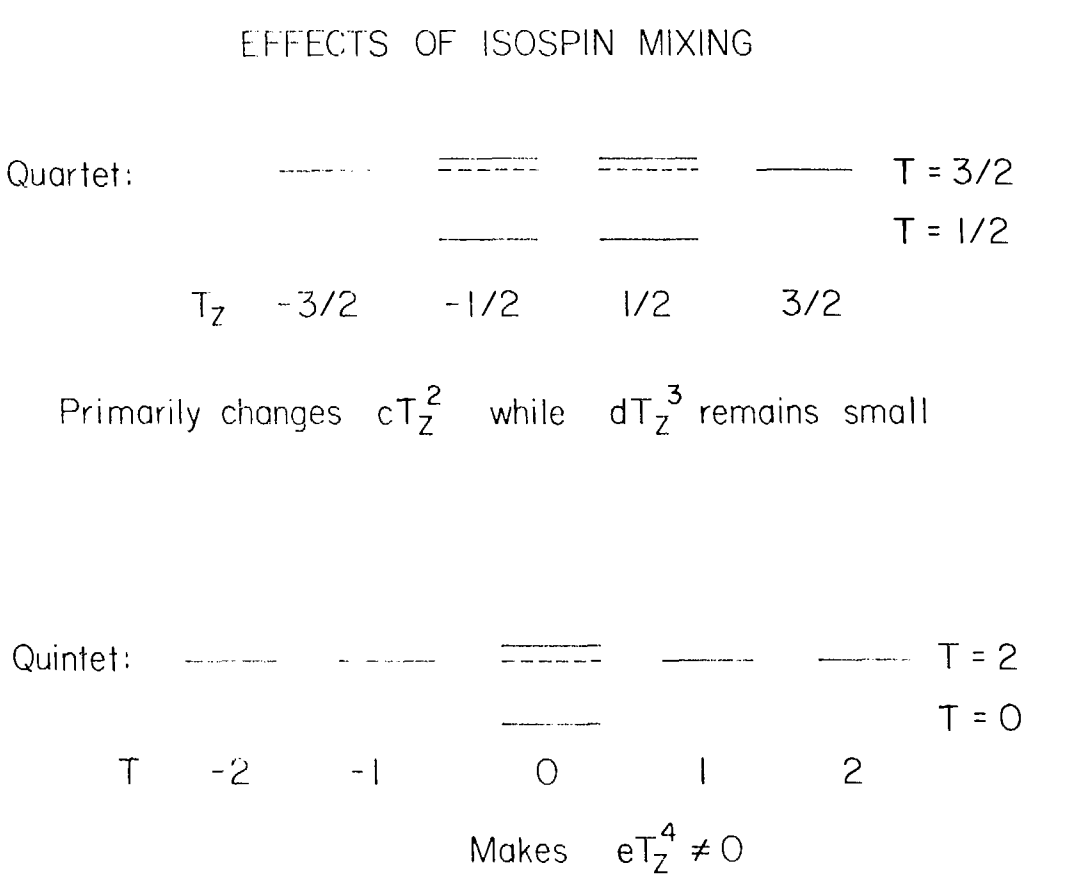

Fig. 2-2. Effects of Isospin mixing in quartets and quintets. XBL 796-1839

IMME Coefficients for a Completed Quintet

$$M = a + bT_z + cT_z^2 + dT_z^3 + eT_z^4$$

$$a = M_0$$

$$b = 1/12\left[8(M_{+1} - M_{-1}) - (M_{+2} - M_{-2})\right]$$

$$c = 1/24\left[16(M_{+1} + M_{-1}) - (M_{+2} + M_{-2}) - 30M_0\right]$$

$$d = 1/12\left[(M_{+2} - M_{-2}) - 2(M_{+1} - M_{-1})\right]$$

$$e = 1/24\left[6M_0 - 4(M_{+1} + M_{-1}) + (M_{+2} + M_{-2})\right]$$

XBL 796-1840

Fig. 2-3. Determination of the IMME coefficients for a completed isospin quintet.

III. Experimental-RAMA

The description of RAMA may be conveniently divided into four distinct parts: the gas-jet, the ion source, the beam transport system, and the detection systems. Each of these topics will be dealt with in terms of those techniques which have been found to work well in the RAMA system. The special problems associated with coupling a gas jet to an ion source will be delineated in addition to problems arising from transport of large beam current (~200 μA). These four main systems may be tied together by considering what happens to a sample nucleus of interest. This radioactive nucleus is produced in a bombardment, recoils from the target (see Fig. 1-1), stops in the helium, attaches to an aerosol, and is subsequently swept through the 6 m long capillary tube away from the region of high background. After exiting the capillary tube with approximately sonic velocity, this aerosol passes through a 1.4 mm skimmer designed to eliminate most of the accompanying helium. Then the aerosol enters the ion source where it is broken up and the radioactive atom ionized to the +1 oxidation state in a gas supported arc discharge plasma. The ion of interest (along with many others) is extracted from the ion source by a 10.5 kV potential. This 10.5 keV particle is then transported through the optics system and collected on the focal plane for decay studies.

A. Helium-Jet

The gas-jet transport method has been studied extensively using several carrier gases with many different additives (Ay 74, Wi 72a,

Wo 77b, and Wi 74). No attempt will be made here to review comprehensively all of the helium-jet methods, only to give details of the technique which has been proven to work for the RAMA system. The helium-jet has been found to work with many additives (Wi 72a and Wi 74) and indeed requires them for efficient transport; experience with the RAMA system is consistent with most of these earlier conclusions. Successful transport of activity has been obtained using acetone, carbon tetrachloride, benzene, methanol, water, ethylene glycol, mechanical pump oil, sodium chloride, and in some cases, small amounts of air. It is now known that these additivies or impurities form large molecular weight clusters or aerosols ranging in size from 10^3-10^8 AMU (Ju 71). In the RAMA system formation of these aerosols requires a sufficient quantity of ionizing radiation (Wi 71 and Wi 73a). In our system, this intense ionizing radiation is created by passage of the cyclotron beam through the helium with an adequate level of radiation being provided by ~1 μA of 40 MeV protons. This beam intensity requirement has been observed to scale roughly as $(dE/dx)^{-1}$ for heavier projectiles (i.e., heavier projectiles have a larger dE/dx and thus, less beam intensity is required for adequate cluster formation).

An additional constraint is placed upon the RAMA helium-jet which is unimportant for most systems. Geometrical considerations for coupling the helium-jet to an ion source dictated that most of the clusters exit the capillary tube in a small forward cone (~2^o opening angle) (Go 72). This requirement for the exiting clusters requires that the aerosols be very massive, 10^6-10^8 AMU. We have

found that only three of the additives mentioned above appear best to meet this criterion: ethylene glycol, mechanical pump oil, and sodium chloride. The latter works well, but if one is not extremely careful in heating the sodium chloride to ~550-600°C, excess quantities of sodium chloride tend to clog the capillary tube. Both of the other additivies work well but ethylene glycol has traditionally been used in our experiments because its vapor pressure curve exhibits large vapor pressure changes with small temperature variations in the room temperature region. This allows us to control its concentration more easily.

Figure 3-1 is a photograph of the helium-jet target box (Se 73b). The water cooled entrance and exit windows are constructed of 2.29 mg/cm² pinhole-free Havar (Ha 73) foil and isolate the 1.3 atm of He from the cyclotron and Faraday cup vacuum systems. The target (shown in Fig. 1-1) is mounted on a movable target wheel directly in front of the copper collection cylinder. A separate set of degrader foils may be placed in front of the target to vary the bombarding energy. Nuclear reaction products recoil out of the target in a forward cone, and are thermalized in the helium. They attach to the high molecular weight clusters and are then drawn toward the capillary opening (on the far side in Fig. 3-1) and transported through the 1.0 mm ID 6 m long capillary tube. The total transit time is ~200ms. (More discussion of transit time may be found in Section F.)

Several perturbations may affect transport of these clusters through the capillary tube. Generally, the helium is entrained in a laminar flow with the interactions of the helium atoms serving to

concentrate the heavy clusters in the center of the flow pattern (An 66). These collisions accelerate the clusters until their axial velocity approaches that of the helium atoms. Upon exiting the capillary tube, these heavy clusters have attained sonic velocity (10^5 cm s^{-1}) and thus, considerable energy and moemntum (relative to thermal molecules). Perturbations to this laminar flow which could either partially or completely eliminate transport include blockages and charge buildup. Blockages are the most detrimental to efficient transport, with tubing kinks and particulate blockages (e.g., ethylene glycol droplets or sodium chloride crystals) being the principal offenders. Charge buildup might be a problem associated with the use of capillary tubes constructed from insulating materials and is avoided in the RAMA system by using annealed stainless steel tubing.

Sonic expansion of a perfect gas expanding isentropically into a vacuum may be treated either as a spherically symmetric flow or as a cylindrically symmetric flow. For the latter, the shape of the gas jet becomes an elliptic paraboloid, and this leads to the simple relationship (Zi 79)

$$\frac{F_z}{F_o} = \frac{s}{B_1 z} \tag{3-1}$$

where F_z is the gas flow rate through a skimmer at a distance z and F_o is the flow rate at the exit of the capillary tube. B_1 is a constant dependent only upon the nature of the gas (B_1 is very large for light masses) and s is the skimmer hole cross sectional area. Simple experiments (Zi 74) have shown that Equation(3-1) holds for our

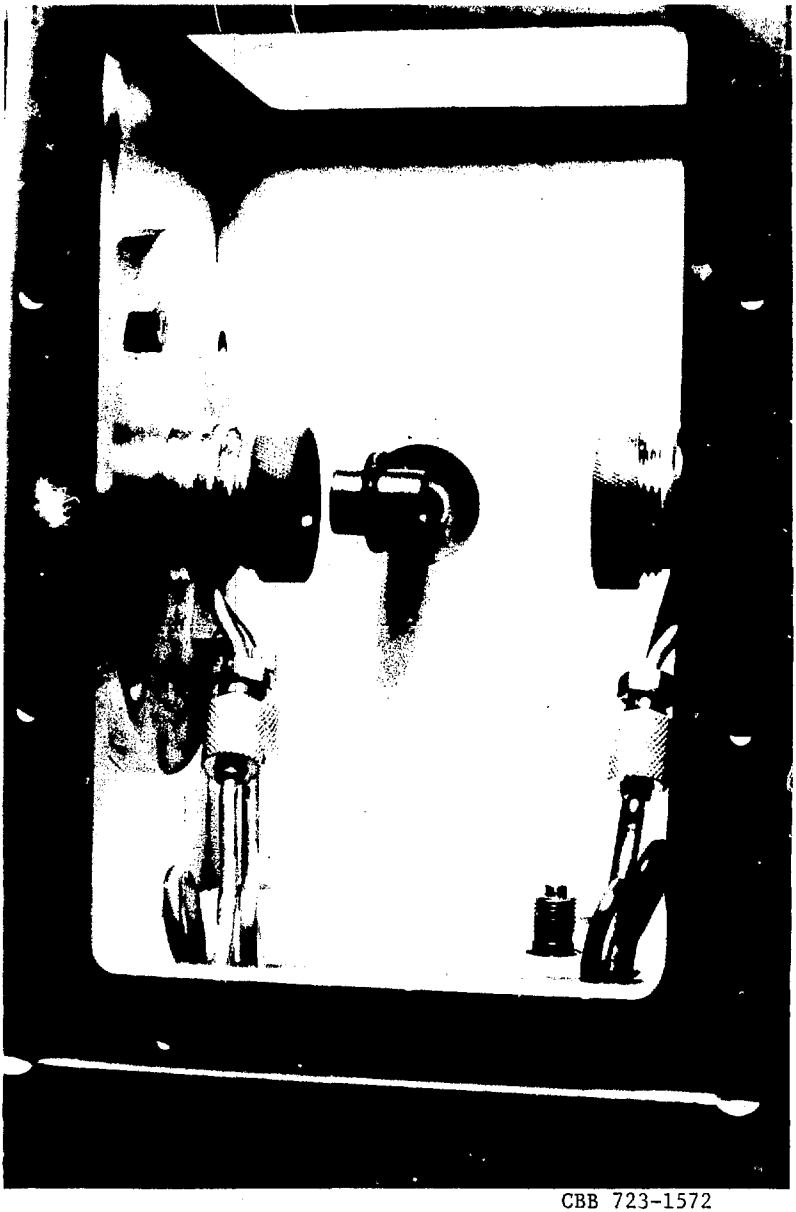

CBB 723-1572

Fig. 3-1. Photograph of the RAMA helium-jet box. The target would normally be directly in front of the collection cylinder.

helium-jet operating conditions. Now if we consider each cluster molecule as an individual entity with no cluster-cluster interactions (the ratio of helium atoms to clusters is 10^{11} - 10^{14}), the clusters can be treated like a very heavy ideal gas. The mass dependent B_1 values (see equation (3-1) for both helium and the clusters are very different, with B_1 for the clusters being very small. This shows why most of the helium strikes the skimmer and is pumped away while most of the clusters pass through the skimmer undeflected.

Shockwave effects must also be considered in the design of a skimmer (Zi 74). Particles exiting a nozzle with sonic velocity create a shock wave which may be reflected from a solid object, and thus, some interference would be expected. A conical shape for the skimmer was originally explored to minimize the effects of this shock wave. Our results concur with those of Schmeing, et al. (Sc 76) and indicate that no appreciable differences exist between conical and flat skimmers. This result is most easily rationalized in terms of the large energy and momentum of each cluster in relation to shockwave distortions in the vicinity of the skimmer orifice.

Use of ethylene glycol with sufficient beam intensities to create clusters generally gives good total transport efficiency; however, the skimmer efficiency varies appreciably (~500%) with our system using a 1 cm axial distance for the skimmer (1.4 mm orifice) and employing a 1 mm ID capillary tube. More reproducibility was observed when cold nitrogen gas-cooled entrance and exit foils were added to increase the beam intensity which could be tolerated on target. These initial

helium-jet inconsistencies were tolerable in RAMA only in the study of high-yield reactions. More details of later improvements developed to increase system reliability are given in Section 3-F.

B. Ion Source

The choice of an ion source for an ISOL system is not easily made because of the great variety of sources which have been tried with varying degrees of success. (See the recent review by Sidenius) (Si 78). For the RAMA system, a source was desired which met the following requirements:

a) acceptably efficient and chemically universal;

b) stable plasma and other operating conditions;

c) short hold-up times.

(A similar set of criteria was investigated by Kirchner and Roeckl (Ki 75, Ki 87a, and Ki 76b) in choosing an appropriate ion source for the GSI on-line mass separator at the UNILAC.)

The type of ion source which appeared to best fit all of these criteria and which could be coupled to the helium-jet was an early Sidenius-type hollow cathode ion source (Si 69). A schematic diagram of the ion source and its holder is shown in Fig. 3-1. The capillary tube separates the target box pressure of 10^{3} torr from the skimmer box pressure of 10^{-1} torr while the large 25 cm diffusion pump further reduces the operating pressure to 10^{-4} torr. A second skimmer on the entrance to the ion source serves to maintain the internal ion source pressure at 10^{-1} torr. A 0.75 mm tantalum filament heats the surroundings and acts as an electron source for the arc discharge maintained between the anode cap (Ta) and the hollow cathode

tubes (Ta). Extraction and acceleration of a beam occurs via the 10.5 kV potential between the plasma and the grounded steel extractor. Steel was chosen for the extractor as well as the ion source housing in an attempt to utilize the large solenoid (crossed area in Fig. 3-2) as a focusing element for the beam as it is being extracted. The extracted beam immediately passes through the Einzel lens which is used to focus the beam into the rest of the optics system.

Normal operating conditions for the hollow cathode ion source consist of a helium supported arc heated by 330±30 W of arc power and 200±20 VA of filmaent power as applied to the 0.75 mm tantalum filament. Its holdup time is ~5 ms at a typical operating temperature of 1800°C. The properties of this ion source have been investigated extensively both with internally produced (off-line) beams and with radioactivity generated by cyclotron bombardments. For certain cases, such as on-line tests with the rare-earth alpha-particle emitter ^{151}Dy (melting point = 1407°C), it appeared that the temperature of the plasma surroundings needed to be significantly above the melting point of the radioactive species, especially when the vapor pressure of an element is very low at its melting point. Extraction of dysprosium ions, for example, only became possible when the filament power was raised to 300 VA. However, the discussion below centers on results determined at the lower filament power (and an extraction potential of 10.5 kV).

Many additional properties of this ion source were defined by tests on the very stable plasma which exists under the arc parameters quoted above. The extracted ion current density is typically

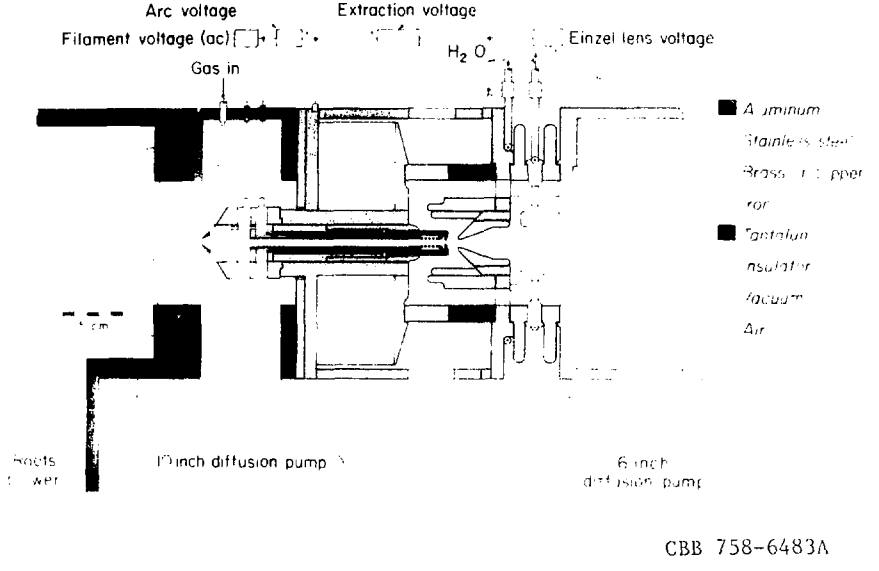

CBB 758-6483A

Fig. 3-2. Schematic diagram of the RAMA ion source region.

300 mA/cm^2 of He^{+1}. Helium is used as the arc support gas because earlier tests with argon and neon as the main support gas gave no yield of Na^{+1}. Tests with argon introduced as a very small impurity in the helium support gas showed the ratio $^{40}Ar^{+1}/^{40}Ar^{+2} \approx 100$. Tests with oxygen under similar conditions showed the O^+/O_2^+ ratio to be ~1000. These two tests demonstrated that, with a helium arc, almost total dissociation of most molecules occurs, with ionization confined primarily to the +1 charge state. Several on-line tests with radioactivity using argon and neon as arc support gases indicated that the charge exchange reaction $He^+ + A \rightarrow A^+ + He$ is the predominant mode of ionization. Our ion source is operated in the anode extraction mode (see Fig. 3-2), and very little activity is extracted ($\leq 1\%$) after the input of radioactive atoms has stopped.

Surface ionization properties of the ion source must also be considered. It was mentioned above that the plasma surroundings must be maintained at a temperature significantly above the melting point. If not, the surroundings behave as a cold-finger vacuum pump and tend to trap the atoms of interest. Once trapped on the cathode surfaces, any activity which ionizes on these surfaces and is subsequently ejected with a positive charge cannot be accelerated into the plasma which is very near the anode potential. Any activity which leaves the anode cap with a positive charge can, however, return to the plasma for extraction. This surface ionization phenomenon is indeed observed with the very volatile and easily ionized alkali metals and will be discussed in greater detail in Section 3-F.

Coupling of an ion source to a beam transport system is necessarily dependent upon the properties of the plasma and the extracted beam characteristics. The latter is best characterized by the emittance which, when measured for this source at the 50% beam level, was found to be 120 mm-mrad for $^{4}He^{+1}$ at 10.5 keV. This emittance was obtained by using a traditional slotted plate technique, and scanned with a scanning wire arrangement discussed in more detail later.

The plasma conditions are determined primarily by four parameters: temperature (T_n) and density (p_n) of the neutral atoms, ion density (p_i), and electron temperature (T_e) (Si 69). The efficiency of an ion source, defined as the ratio of atoms ionized compared to the number introduced, is given in terms of the above parameters as

$$n_i = \left(1 + \frac{p_n}{p_i} \sqrt{\frac{T_n}{T_e}}\right)^{-1} . \qquad (3\text{-}2)$$

Equation (3-2) shows that for a particular type of ion source, the temperature of the electrons and the ion density need to be kept as high as possible. The electron temperature is governed by the arc voltage (~230 Volts) while the ion density is primarily governed by the electron density (for a given density of neutral atoms). The filament is the primary electron source and, therefore, the choice of material is important. Originally filaments were constructed from 0.75mm tantalum wire, which lasted ~85 hrs at 200 VA (but which evaporated rather quickly (~8 hrs) at filament powers of 300 VA). Improved results were obtained with filaments constructed from either

0.50 mm or 0.75 mm tungsten. The tungsten filaments give operating times of ~200 hrs at 200 VA (and ~50 hrs at 300 VA). To improve the overall reliability of this ion source, the tantalum cathode and anode pieces have been converted to molybdenum. Molybdenum was chosen because of its greater structural strength and its nearly identical coefficient of thermal expansion to that of tungsten.

The plasma is strongly affected by the solenoidal magnetic field created by the current passing through the filament. This field is significant (100-150 gauss) and does not permit the operation of the source with helium as a support gas when the magnetic field is monodirectional (DC filament supply) and unsuppressed. Although the addition of an external solenoid can make the effective field in the plasma region zero, our solution has been even simpler. We use an AC filament supply (60 Hz). This effectively extends the lifetime of electrons in the plasma which increases the electron density, and thereby increases the efficiency. No resolution degradation is noted due to this type of operation. Changes in the arc conditions change the observed resolution minimally while changing the magnetic field dramatically worsens the resolution.

The ions are extracted from the ion source and accelerated to their final energy of 10.5 keV by a simple conical grounded extractor electrode placed at distances of 5-10 mm (variable). The extractor is constructed from structural steel because it was hoped to use the focusing solenoid shown in Fig. 3-2 to increase the amount of beam output of the ion source. Tests with this solenoid succeeded only in

extinguishing the arc and thus it was never used in actual experiments. This ion source, as coupled to the rest of the mass separator, meets most of the criteria desired: a) chemically universal for elements with melting points below 2000°C; b) very stable plasma conditions for long periods of time (days); c) short hold-up times (<5ms). The major drawback of this hollow cathode ion source is the low yield of elements whose melting points exceed 2000°C. One method to improve this efficiency would be to increase the electron temperature and density.

The measured efficiency for the ion source of 0.1 - 0.2% taken together with the ~10% efficiency for the rest of the system in principle permits us to observe ~75% of all elements produced with cross sections from 0.1 mb to 50 mb depending upon whether one is observing discrete energy charged particle decays or doing beta or gamma spectroscopy. These cross section limits are derived by considering the efficiencies in Table 3-1 (discussed further below) in relation to typical counting rates necessary for different types of experiments. The number of observable elements is based on the relative number of volatile elements with melting points ≤2000°C.

C. Beam Transport

Several factors need to be considered in designing an appropriate beam transport system for low energy beams. In the context of the RAMA design, complications arise because of the large extracted He^{+1} currents (100-200 μA) which can give rise to detrimental space charge effects with 10.5 keV beams. To eliminate the huge helium beam

Table 3-1. RAMA efficiencies

	^{20}Na	^{111}Te	^{150}Dy	^{211}At
He-jet	20%[a]	60%	10%[a]	15%[a]
Skimmer	70%	60%	60%	70%
Ion Source	$0.2_{3\%}$	$0.1_{2}\%$	~0.2%	0.2%
Magnetic Analysis[b]	50%	50%	50%	50%
Overall	0.016%	0.02%	0.01%	0.01%

a) Not optimized.

b) Caluclated based on measured ion source emittance.

current, a Wien filter (see Fig. 1-1) is employed. The Wien filter is tuned for the mass of interest while deflecting the $^{4}He^{+1}$ away from the rest of the optics system.

In order to maximize the beam through the Wien filter, the beam is focused by an Einzel lens (see Fig. 1-1) maintained at a potential only slightly less (typically 9.5 kV) than the extraction potential (10.5 kV). The Einzel lens voltage is critical in that it determines the spot size through the Wien filter and, thus, the ultimate resolution. Before entering the Wien filter, the beam passes through a drift tube. In this region stray helium beam collides with the tube walls which eject electrons that mingle with the beam and effectively reduce space charge blowup. A suitable tube size was determined by measuring the $^{40}Ar^{+1}$ beam focused through the Wien filter as a function of tube radius (these electrons are not transmitted through the Wien filter.).

Although the Wien filter magnetic field is relatively inhomogeneous with significant fringing fields, this does not cause a problem since it is operated at a constant magnetic field (while tuning the electric field). However, it was necessary to use an indirect method to establish the effective magnetic field. This was accomplished by determining the electric field needed to center the mass of interest versus $m^{-1/2}$ for several different beams. The slope of a plot of results is equal to $B_{eff}\sqrt{2E}$, where E is the beam energy, so that electric field settings could easily be calculated for any mass. Sample RAMA calculations may be found in Appendix C. Another requirement observed in later tests showed that the helium deflection

angle needed to be between 4^{o} and 12^{o}. The 12^{o} limit is required to keep the helium beam from striking the electric field plates of the Wien filter while the 4^{o} limit is required to keep the helium beam from entering the remainder of the transport system. The resolution is dramatically worsened if these limits are exceeded.

The rest of the transport system (Fig. 1-1) was designed around a desired mass resolution $M/\Delta M$ of ~200, a normal focal plane, a mass range of ±10%, and a double focus on the focal plane. The beam at the center of the Wien filter is treated as the virtual source for the optics. Calculations for this beam transport system were performed using standard electromagnetic formalism (Se 75, Ba 66, Re 67, and He 74). The first order calculations employ an electrostatic quadrupole triplet system (whose first and third elements operate together) to match the ion source emittance to the acceptance of the dipole analyzing magnet. (At low energies magnetic and electrostatic quadrupoles work equally well, but an electrostatic quadrupole may be tuned independently of the ion mass, making it the preferred choice.) Because of the availability of a surplus cyclotron beam bending magnet, a 75.5^{o} separator was designed.

A solution to the ion optics was obtained which transmitted 50% of the ion source output (based on the measured emittance) to the focal plane at the desired resolution of $M/\Delta M$ ~200. A central ray of the beam entering the dipole magnet is bent 75.5^{o} and traverses entrance and exit edge angles of $\beta_1 = \beta_2 = 11^{o}$. A double focus was obtained on the focal plane with a small magnification in the x (radial) direction (M_x~0.5) and a large magnification in the y

(vertical) direction ($M_y \sim 1.2$). Such a large value for M_y poses no problem so long as neither collector nor detector dimensions are exceeded. A dispersion of 1.62 m was also calculated.

Second order calculations showed that second order aberrations were non-negligible. The beam is cylindrically symmetric with a divergence of ~30 mrad in both the x and y dimensions. This cylindrical symmetry created a need for both an upstream sextupole (SXT 1) and an entrance edge sextupole (there is no exit edge sextupole) because a gain in one dimension caused an equivalent loss in the other dimension for a single sextupole system (see Fig. 1). If we denote the properties of a ray entering the dipole magnet with the vector notation of (x, x', y, y') where x and y are displacements and x' and y' are angles, then we may write the central ray as (x_o, x_o', y_o, y_o'). Since in our case $x_o' >> x_o$ and $y_o' >> y_o$, then the most important second-order aberrations are represented by terms in which x_o' and y_o' appear. The upstream sextupole and the entrance edge sextupole serve to minimize the largest second order matrix elements, namely the coefficients of the $(x_o')^2$ and $(y_o')^2$ terms.

To minimize the effects of the fringing field from the dipole magnet and to insure a well defined entrance edge sextupole, field clamps were installed. Field maps of the dipole magnet were obtained by a standard computerized mapping procedure (Do 72), providing a determination of the effective field boundary which was then used as input for the final optics calculation. The field maps also showed that the homogeneity of the magnet was sufficient to make shimming

unnecessary. The second order calculations also showed that the focal plane angle was rotated 61^{o} to the ion trajectories which was deemed to be inconveniently steep. A downstream sextupole (SXT 2) was therefore incorporated to rotate the ±10% mass range focal plane normal to the beam (or z) direction.

Extensive measurements of the beam properties on the RAMA focal plane were performed with internally produced $^{40}Ar^{+}$ beams. Figure 3-3 presents data on these properties as various optical elements are introduced. These scans were obtained on the center plane of the detector box (see Fig. 1-1) with a simple scanning wire arrangement connected to an x-y recorder; this beam current was measured as a function of either horizontal or vertical distance. The resolution values are all quoted at FW.1M (full width at one-tenth maximum) and are calculated from the equation $\mathrm{Res}(M/\Delta M) = \frac{D}{Zw}$ where D is the dispersion and w is the measured peak width at one-tenth maximum. The first curve in Fig. 3-3 shows that very little beam was obtained when no elements except the dipole magnets were operative. Turning on the quadrupole triplet and the Wien filter gave a large increase in transmitted beam and a resolution of ~90. When next the downstream sextupole was turned on (third scan in Fig. 3-3), the focal plane was rotated to become normal to the z-axis with virtually no effect on the resolution is noted. The fourth curve in Fig. 3-3 shows the dramatic improvement in resolution (to ~195) when the upstream sextupole was turned on. This overall measured resolution compares well with the calculated value of 190. Further tests showed that the actual dispersion was 1.64 m (calculated 1.62 m)

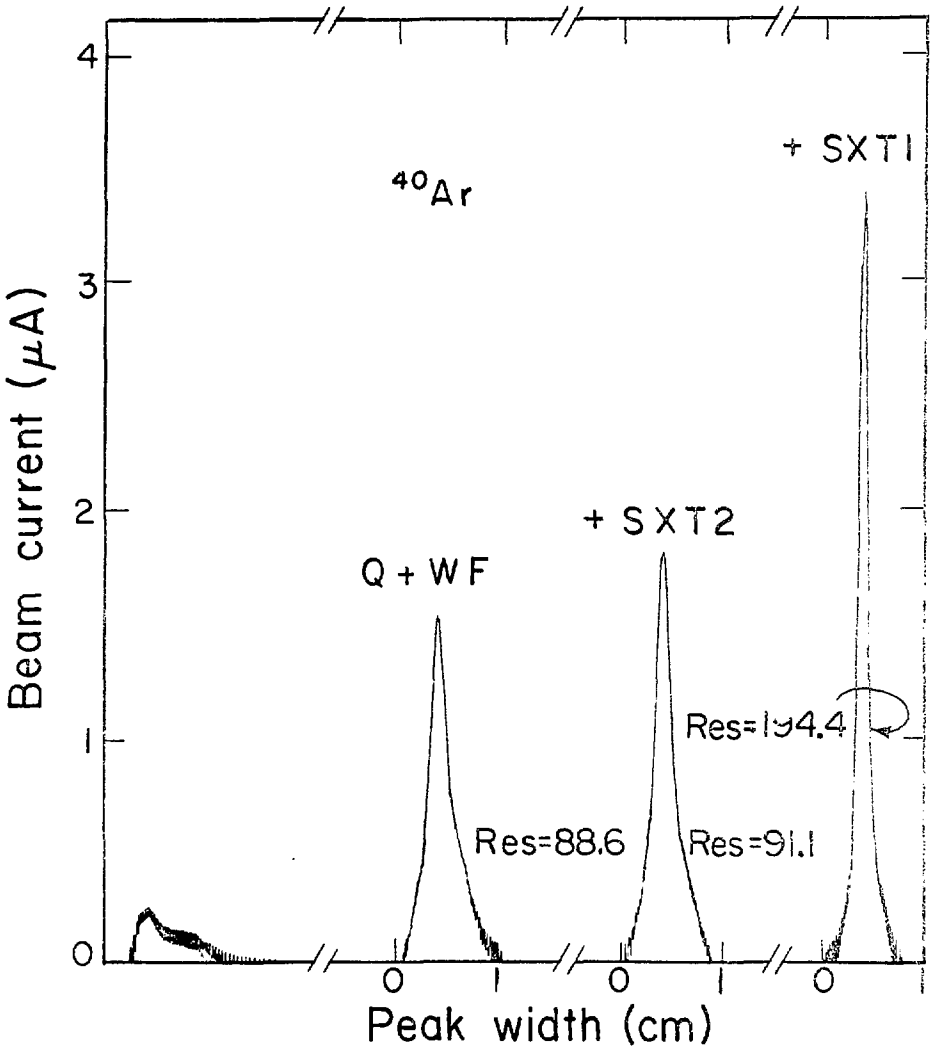

XBL 7612-4594

Fig. 3-3. Effects of various optical devices on an $^{40}Ar^{+1}$ beam as horizontally scanned on the center-line of the RAMA focal plane. More details are given in the text.

for the central ray. This dispersion varied from 1.68 m on the high mass side to 1.60 m on the low mass side of the ±10% mass range of the focal plane.

For general on-line beam tuning, the scanning wire arrangement is not useful because its requires microamp current levels which are often inconveniently high and requires special arc support gas mixtures. Therefore, a channeltron electron multiplier (CEM) was installed on the center-line of the focal plane to permit tuning of the optics at more realistic beams levels (say 100-50K Hz). Basically, the channeltron electron multiplier produces an electron cascade for each charged particle that strikes its detection cone, yielding a current gain of 10^5-10^7; this current pulse is then collected on a Faraday cup and measured by a picoammeter. This system allows us to tune RAMA with the ^{40}Ar gas impurity contained in the helium arc support gas, and to a lesser extent, with the ubiquitous ^{39}K. It also permits the introduction of heavier, less volatile elements at a sufficiently low level to avoid affecting the operation of the ion source. For example, tin can be introduced into the arc support gas by passing it over the non-volatile liquid tetraethyl tin(IV) (BP ~182°C), thereby providing a unique isotopic signature. This technique is very useful for calibrating RAMA in situ after the system has been operating for some time without disturbing the existing setup.

D. Detection Systems

Initial considerations in the design of a detector station were to provide maximum versatility for the wide variety of experimental arrangements anticipated. A detector box with a large number of ports

was fabricated, necessitating large pumping capacities to maintain the detector box base pressure of 1×10^{-6} torr. Because of the large helium leak associated with the ion source, the normal operating pressure is 3×10^{-6} torr.

To separate adjacent masses, a movable slit system was designed. The slit width may be continuously adjusted from 0-20 mm about a movable point in the x-direction of the 16 cm focal plane. Rolling collimators attached to the slit arms keep activity from other masses from reaching the detector systems. Although only one system is normally employed in the center position, a second independent system can be used for studying a second mass position. Once the radioactivity of interest passes through the slits, it is collected for decay studies. One method of collection consists of stopping activity on a thin (300 $\mu g/cm^2$) aluminized polycarbonate foil mounted directly in front of either a single solid state detector or a detector telescope mounted on a movable arm. The actual detector mounts are electrically isolated and may be thermoelectrically cooled to temperatures approaching $-40^{\circ}C$.

The collection and detection method described above is not optimum for decays involving heavy charged particle production because of the large energy loss (50-500 keV) of protons and alphas as they pass through the collector foil and the resulting peak broadening. This problem is overcome with a flipper wheel system shown schematically along with an operational sequence in Fig. 3-4. The flipper wheel arrangement permits only previously collected activity to be viewed by the appropriate solid state detector system. Though the flipper wheel

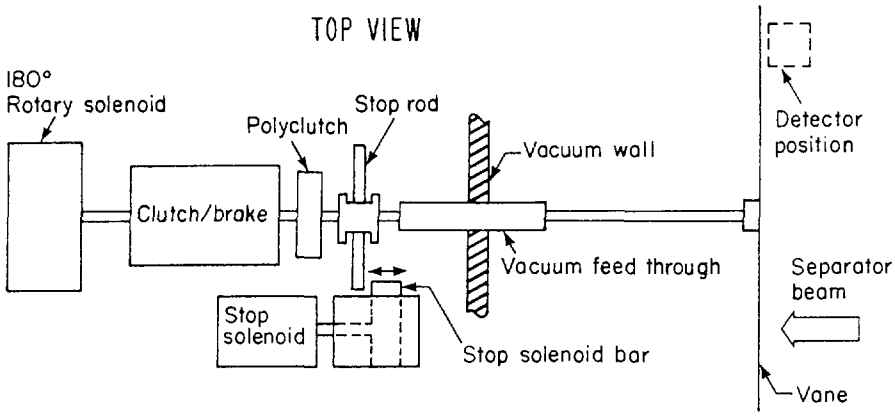

SEQUENCE OF EVENTS:

1) CLUTCH/BRAKE ENERGIZED TO CONNECT ROTARY SOLENOID TO SHAFT.

2) ROTARY SOLENOID ACTUATED ROTATING SHAFT 180°.

3) STOP SOLENOID ENERGIZED AFTER SHAFT HAS ROTATED ~ 90° PULLING STOP IN PATH OF STOP ROD.

4) AFTER TRAVELLING 180°, CLUTCH/BRAKE DE-ENERGIZES STOPPING ROTATION AND ALLOWING ROTARY SOLENOID TO RELAX.

5) STOP ROD HITS STOP SOLENOID BAR AFTER TRAVELLING EXACTLY 180°.

6) STOP SOLENOID RELAXES.

7) POLYCLUTCH ALLOWS ROTATION ONLY IN ONE DIRECTION PREVENTING BACK-SPIN WHEN STOP ROD HITS STOP SOLENOID BAR.

Fig. 3-4. Schematic diagram of the flipper wheel system. The sequence of events involved with a single 180° rotation is also listed.

system is very fast, rotating and stopping in approximately 40 ms, its stopping is inherently violent, creating a situation whereby only 1000-2000 flips are obtainable before some sort of realignment becomes necessary. Thus, it is not readily adaptable for activities with half-lives below 30 s. More reliability could easily be achieved by increasing the rotation time.

E. Initial Tests with Radioactivity

Initial tests of the RAMA system were performed with the beta-delayed alpha-particle emitter ^{20}Na, produced via the ^{24}Mg(p,αn) reaction at 38 MeV, due to its easily identifiable alpha groups and its short half-life of 446 ms. These tests included checking all of the optics parameters relative to calculated values based on the higher beam current scans of $^{20}Ne^{+1}$. Further tests of the RAMA system were performed with the much heavier nuclide ^{211}At ($t_{1/2}$ = 7.2h). This alpha-particle emitter was produced via the ^{209}Bi(α,2n) reaction at 27 MeV. A scan of the mass 211 region with data from the alpha-particle decays of ^{211}At and its daughter, ^{211}Po, is shown in Fig. 3-5. The measured resolution of 205 was consistent with the off-line mass scans, and indicated that RAMA could be operated on a stable basis for many hours.

After these initial studies were completed, several more comprehensive tests were desired for the RAMA system. The light N = 84,85 rare-earth alpha-particle emitters, copiously produced in (HI, xn) reactions, were chosen because of their relatively short half-lives and their easily identifiable alpha groups. In addition, the mass of a number of the shorter-lived (< 1 min) rare-earth alpha-particle

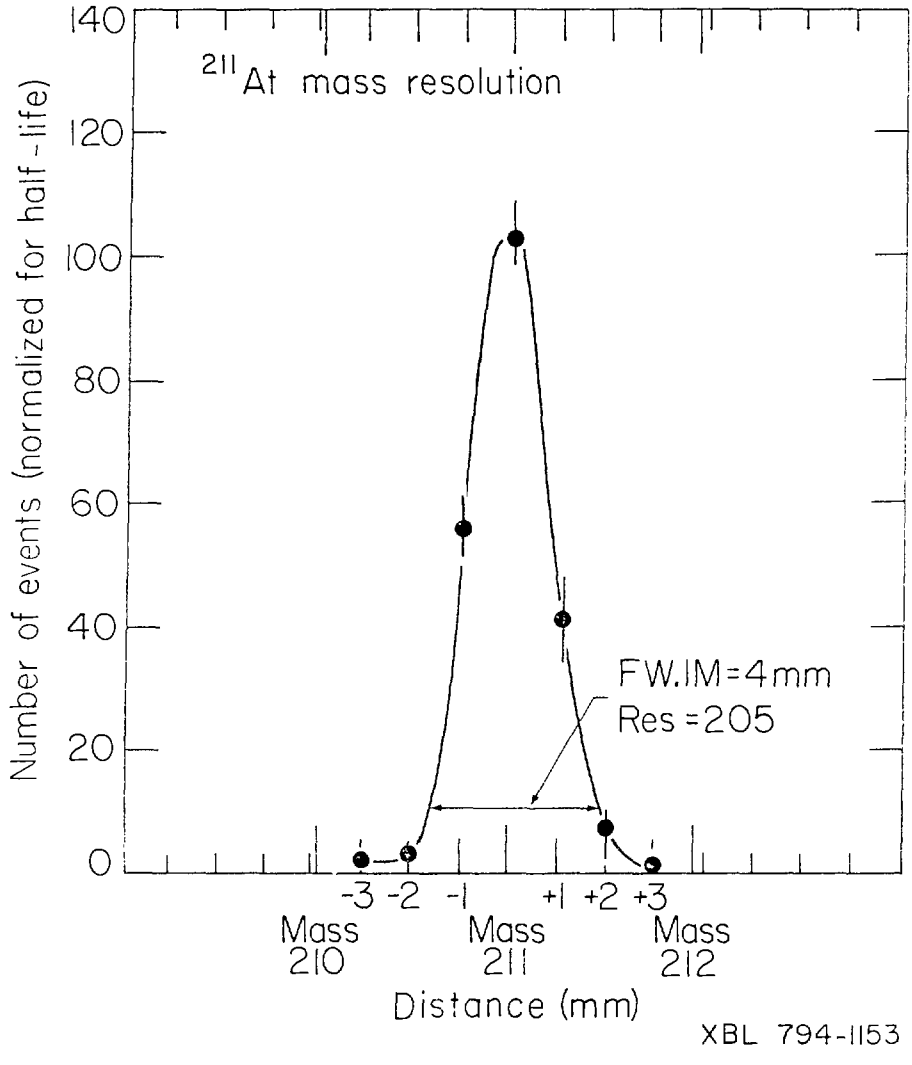

Fig. 3-5. Scan of mass 211 using the alpha-particle emitter ^{211}At produced by the ^{209}Bi(^{12}C,2n) reaction at 27 MeV.

emitters had only been established by systematic relationships, without any absolute verification. Initially, the well-known ^{150}Dy and ^{151}Dy isotopes were observed, produced in $^{142}Nd(^{12}C,xn)^{154-x}Dy$ reactions at 78 MeV, as was $^{149}Tb^{g}$ produced in the ^{142}Nd (^{11}B,4n) reaction at 62 MeV and in the $^{141}Pr(^{12}C,4n)$ reaction at 78 MeV. Then, the masses of many of the light short-lived N = 84,85 isotones were determined in a series of experiments involving bombardments of ^{140}Ce, ^{141}Pr, ^{142}Nd, and ^{144}Sm targets with ^{11}B, ^{12}C, ^{14}N, and ^{16}O beams at various energies. These targets were in the form of oxides and nitrates supported by either copper or nickel backing foils. A typical alpha-particle spectrum collected on the flipper wheel and measured with a large surface barrier detector is shown in Fig. 3-6 while Table 3-2 summarizes our results compared to the literature assignments (Ga 75). These results confirmed the mass assignments of most of the short-lived rare-earth alpha-particle emitters between holmium and ytterbium. Figure 3-7 presents a spectrum which confirmed the masses of both the high-and low-spin isomer of ^{151}Ho. Such a confirmation has been independently made in recent work by Hagberg, et al. (Ha 77a) at ISOLDE in which decay studies of mass separated samples of ytterbium were observed in addition to subsequent daughter decays.

A second experiment of interest was motivated by the assignment of a 19 s beta-delayed proton activity to ^{111}Te by Bogdanov et al. (Bo 68a and Bo 68b) and to ^{110}Te by Macfarlane and Siivola (Ma 64). Both of these assignments were initially based solely on excitation function and cross bombardment data. Figure 3-8 shows that a proton

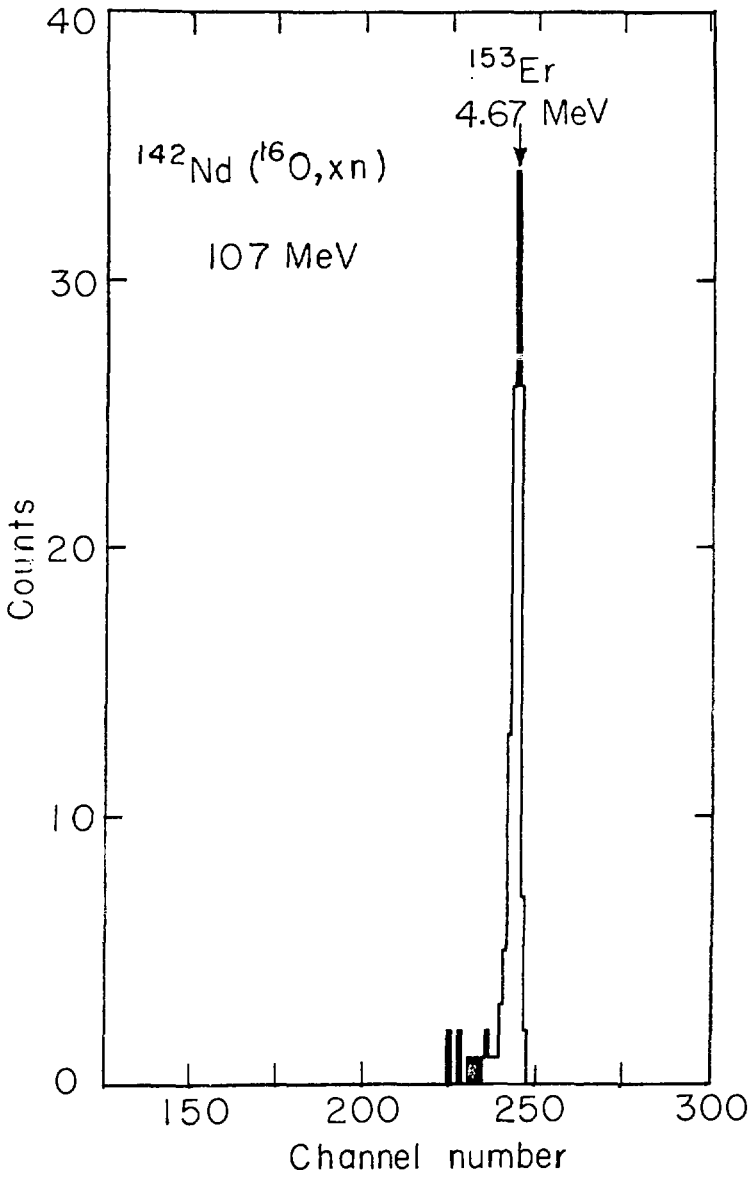

Fig. 3-6. ^{153}Er alpha-particle spectrum at the mass 153 position on the RAMA focal plane produced by the ^{142}Nd(^{16}O,5n) reaction.

Table 3-2 Rare-earth alpha-particle emitter mass confirmations.

Nuclide	Z	Alpha Particle Decay Energies (MeV) Observed[a]	Literature	$t_{1/2}$ Observed	Literature[b]
$^{149}Tb^{g}$	65	3.95	3.95	4.07 ± 1.0 h	4.1 ± 0.2h
^{151}Dy	66	4.07	4.07	17.5 ± 0.5 m	17.7 ± 0.5m
^{150}Dy	66	4.23	4.23	7.1 ± 0.7 m	7.2 ± 0.1m
^{152}Ho(High Spin)	67	4.45	4.46	53 ± 4s	52.3 ± 0.5s
^{152}Ho(Low Spin)	67	4.38	4.38	2.0 ± 0.5 m	2.36 ± 0.4m
^{151}Ho(High Spin)	67	4.51	4.52	36 ± 2 s	35.6 ± 0.4s
^{151}Ho(Low Spin)	67	4.60	4.60	37 ± 8 s	42 ± 4s
^{153}Er	68	4.68	4.67	35 ± 2 s	36 ± 2s
^{152}Er	68	4.82	4.80	-	9.8 ± 0.3s
$^{154}Tm^{m}$	69	5.02	5.04	-	3.0 ± 0.2s
^{155}Yb	70	5.19	5.21	-	1.65 ± 0.15s
^{154}Yb	70	5.32	5.33	-	400 ± 4.0ms

a) Typical errors are ± 0.03 MeV.

b) Ref. (Ga 75)

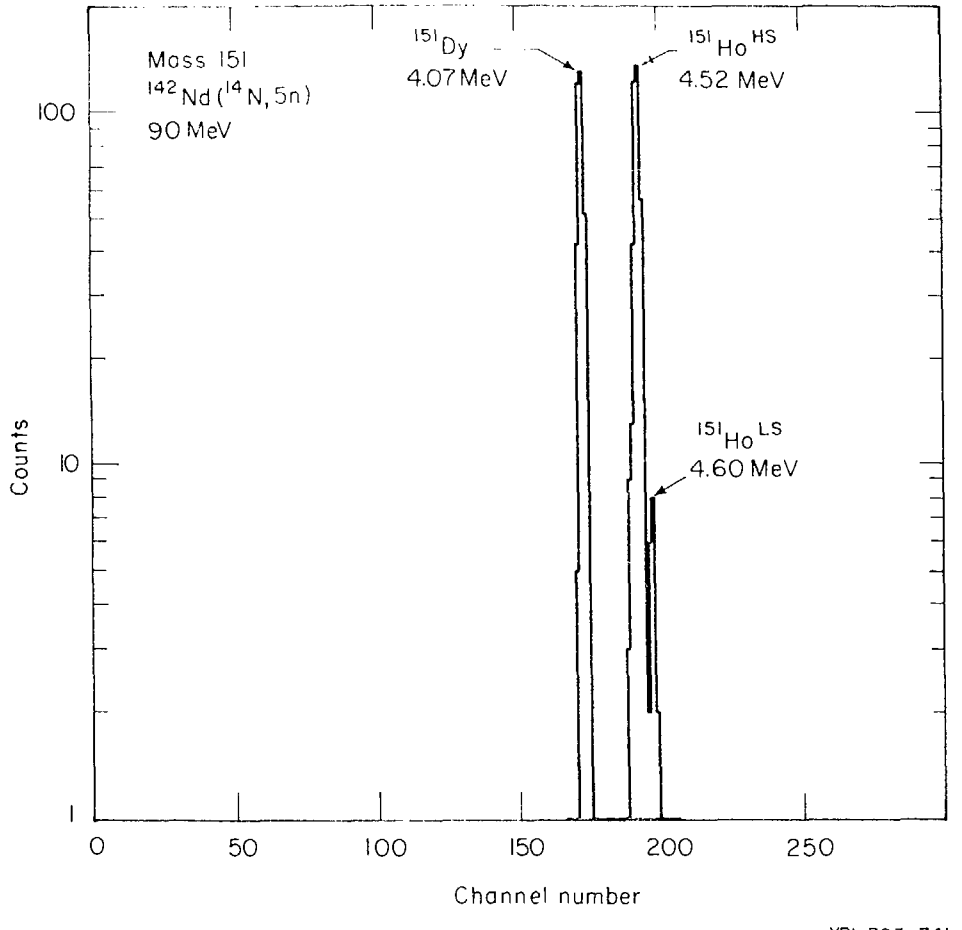

Fig. 3-7. Alpha-particle spectrum resultant from ^{14}N reaction with ^{142}Nd at the mass 151 position with a 90 MeV bombarding energy.

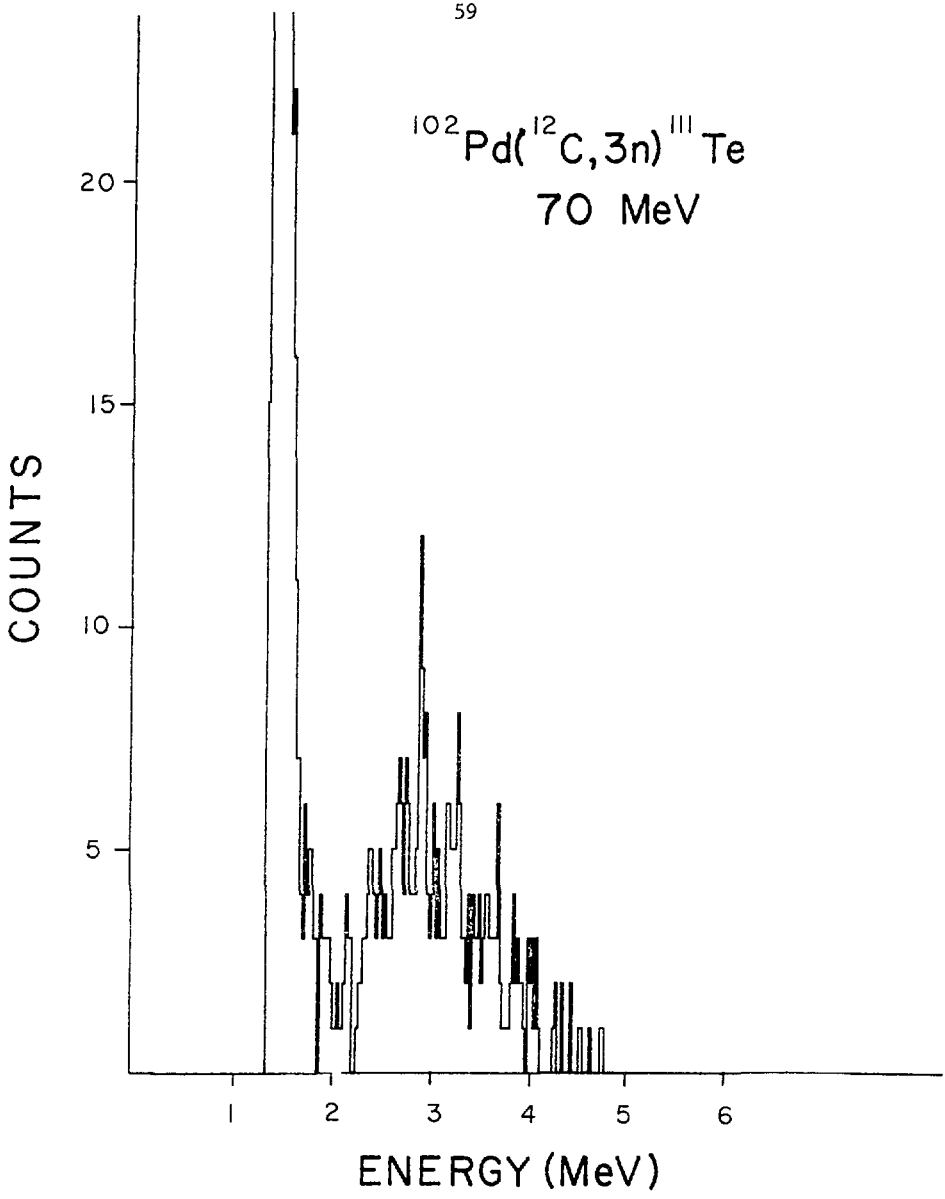

Fig. 3-8. Proton spectrum at the mass 111 position from ^{111}Te produced by the ^{102}Pd(^{12}C,3n) reaction at 70 MeV.

spectrum obtained at the mass 111 position which coincides with that previously observed for this 19 s activity, clearly assigning it to the decay of ^{111}Te; this result has been separately confirmed by work reported from UNILAC (Ke 77 and Ro 77a). Further studies (Ki 77) in this region have led to our observation of delayed protons from ^{109}Te and ^{112}I produced by the ^{102}Pd(^{12}C,5n) and ^{102}Pd (^{14}N,4n) reactions, respectively; these results agree with similar data reported by Kirchner, et al.(Ha 77a). The study of these various elements with vastly different chemical properties and half-lives demonstrates the versatility of RAMA. A summary of the overall observed efficiencies for four of the activities mentioned above as a function of their transmission through the various components of the RAMA system may be found in Table 3-1.

F. Changes in RAMA

The versatility of the on-line mass separator RAMA has already been demonstrated. The basic system, however, had some features which made its operation less than ideal. It was evident that the operating conditions of the helium-jet system had not been totally optimized. Further the ion source was excessively long, making the acceptance of the skimmed activity cone necessarily small, and the accelerating and extracting potential could not be maintained above 11 kV without breakdown of primary insulators. Since the overall efficiency of the RAMA system was only ~0.01%, it was clearly of interest to improve the operating conditions.

One of the original objectives of the RAMA system was to study the decay of the A = 4n, T_z = -2 series of beta-delayed proton emitters

utilizing the (^{3}He,3n) reaction. In the search for ^{40}Ti by Sextro, et al. (Se 74), only protons from the well-known beta-delayed proton emitters ^{37}Ca and ^{41}Ti produced in much higher yield in the competing (^{3}He,α2n) and (^{3}He,2n) reactions were observed. Mass separation was thus needed. The (^{3}He,3n) reactions were expected to have production cross sections such that effective observable cross sections of 1μb were of interest. Considerable improvement in total yield was thus needed to make these studies possible. Though our discussion will continue to use the search for these beta-delayed proton emitters as an example, the ability to observe low yield, short half-life species is of general interst in the study of nuclei far from stability.

Two areas were considered as obvious candidates for improvement, the helium-jet and the ion source. Figure 3-9 presents a schematic diagram of the RAMA system with these changes. The first improvement was the addition of a multiple capillary system with a cooled collection cylinder and nitrogen gas cooled entrance and exit windows. The second major improvement was a total redesign of the ion source region including shortening the ion source by more than a factor of two. This section will center primarily on discussing these two improvements in addition to a brief account of the new detector systems developed for studies of the quite short-lived (~100 ms) T_Z= -2 beta-delayed proton emitters.

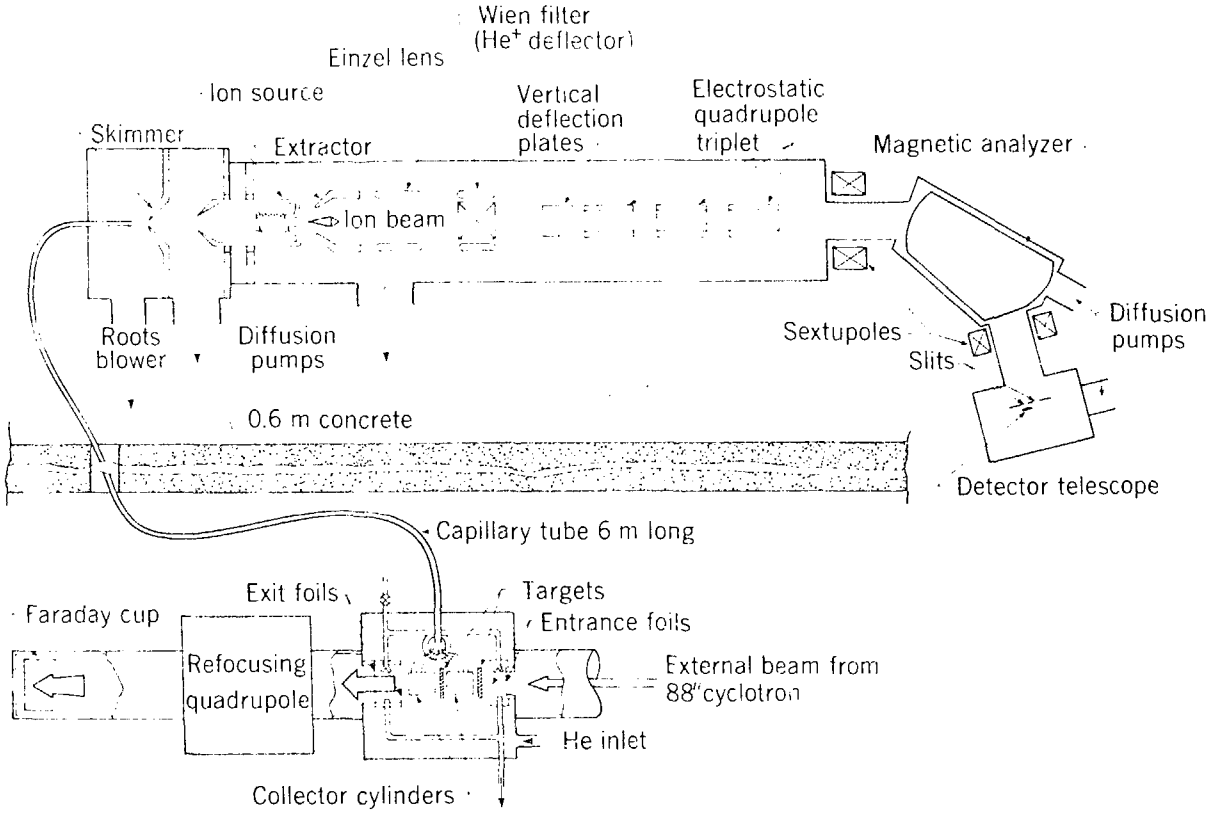

Fig. 3-9. Overall schematic diagram of the present RAMA system.

1. Multiple Capillary System

In a traditional one-capillary gas-jet system, the total transport yield for short-lived ($t_{1/2}$ < 500 ms) and long-range (> 1 cm) recoil atoms is limited due to the large gas volume needed to stop the recoils. Since many light nuclei far from stability have half-lives in the 100 ms regime, improvements to increase the yield of short-lived activities from the helium-jet system had to be considered. A multiple capillary system was designed for both gas and solid targets to decrease the active collection volume in the target- capillary space as well as to increase the total target thickness for optimum recoil production.

The proposed multiple capillary system for gas targets is shown schematically in Fig. 3-10. In this case, the transport gas also serves as the target medium. Nuclear reaction recoils are thermalized in the collection cylinder, collected by a set of adjacent capillaries spaced evenly in the side of this cylinder, and then sent to a junction. A single 6 m long stainless steel capillary transports the activity from the junction to the skimmer-ion source region. The total yield exiting from the helium-jet system is given by

$$\text{YIELD} \quad Y = \sigma' \cdot N \cdot \Delta V_o \, e^{-\ell n 2 (t_d / t_{1/2})} \tag{3-3}$$

where t_d = the total delay time

$t_{1/2}$ = half-life of the activity of interest

ΔV_o = active collection volume per capillary

N = number of capillary tubes

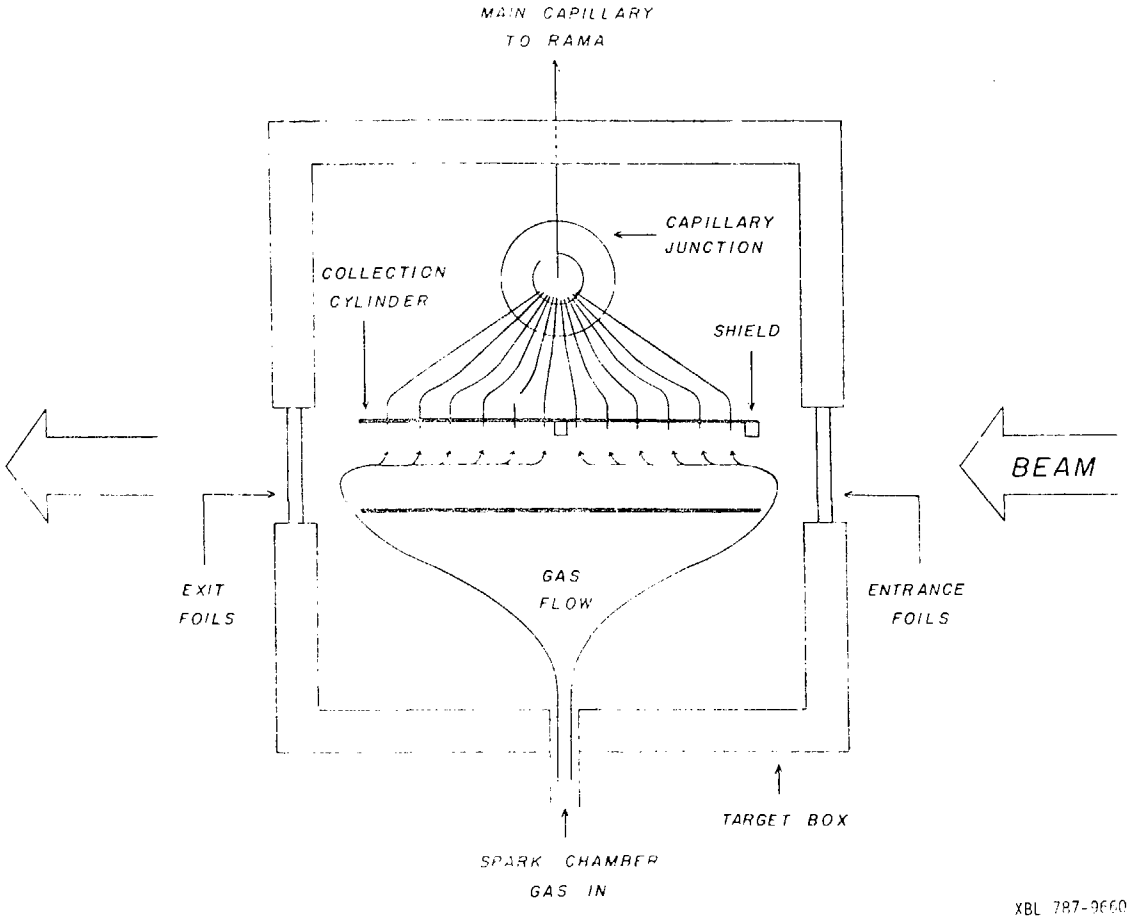

Fig. 3-10. Schematic diagram of the gas target multiple capillary system.

σ' ≡ the effective cross section thermalized in ΔV_o.

The total delay time is a sum of the effective sweep-out time of the total collection volume $N \cdot V_o$, of the multiple capillary delay time, and of the delay time in the main capillary tube. It is given by

$$t_d \approx \frac{N \cdot \Delta V_o}{Q} + \frac{N \cdot \bar{L}_M}{\bar{v}_m} + \frac{2L}{3v_o} \qquad (3\text{-}4)$$

where Q ≡ flow rate

$\bar{L}_M$ ≡ average capillary length in the multiple capillary system

$\bar{v}_m$ ≡ average gas velocity in the multiple capillary system = $4Q / N\pi D_M^2$

L ≡ length of the main capillary

v_o ≡ initial gas velocity in the main capillary

D_M ≡ diameter of a capillary in the multiple capillary.

The approximation stems from the approximation $\frac{2L}{3v_o}$ (Da 73) and from ignoring the very small delay time in the junction. If we assum $L_M << 0.01L$ and $D_M \sim D$ (D is the diameter of the main capillary tube), the delay time in the multiple capillary system is small and the total delay time can be approximated by

$$t_d \approx \frac{1}{Q} \left[\frac{\pi}{6} L D^2 + N \Delta V_o \right] . \qquad (3\text{-}5)$$

An illustration of the yield as a function of capillaries and the species half-life is given in Fig. 3-11. By substituting either measured quantities or reasonable estimates for all the parameters, the curves for two different 6 m long capillary tubes (1.0 and

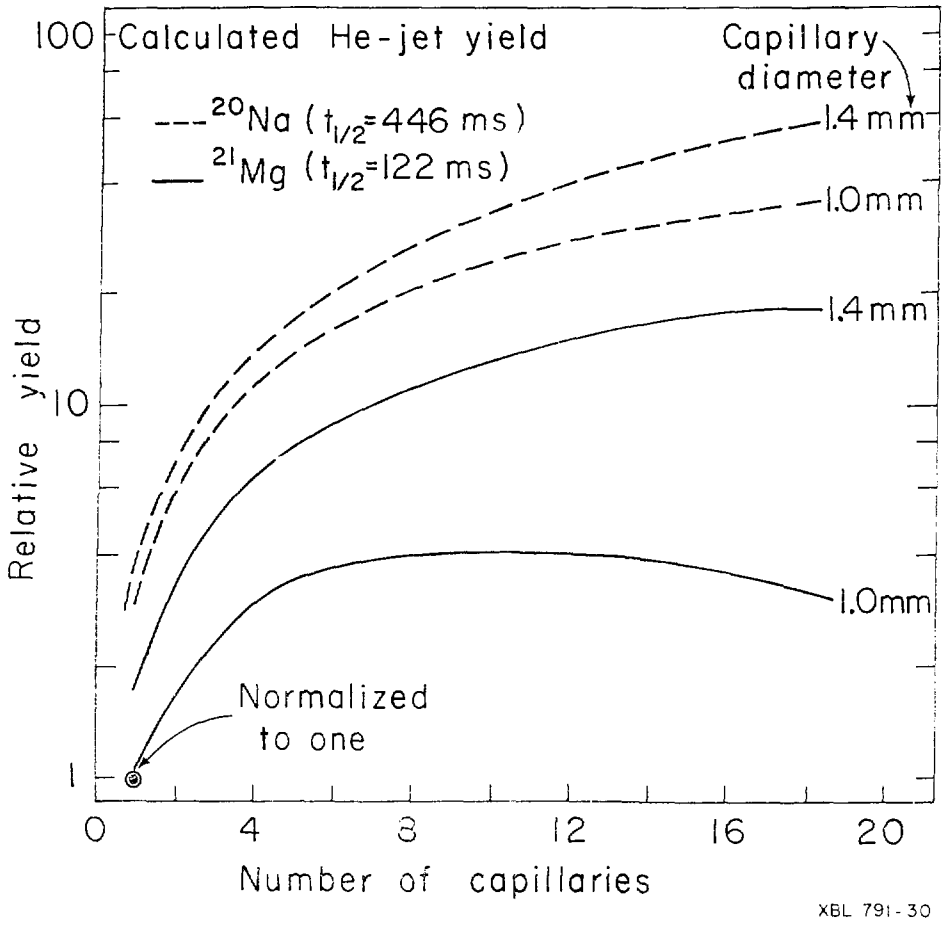

Fig. 3-11. Theoretical yield for a short-and a longer-lived activity as a function of the number of capillary tubes in a multiple capillary system. Calculational details are given in the text.

1.4 mm ID) for two different half-lives are obtained. For very short-lived activities, the increased production is offset by the increased transport times associated with a multiple capillary system.

For example, the calculation for a 1 mm ID capillary show that the yield for a nuclide with a 122 ms half-life (^{21}Mg) increases by a factor of four when a single capillary is replaced by a ten-capillary system. An overall increase of 10 results when the same ten-capillary system feeds a 1.4 mm main capillary tube. These calculations were experimentally checked with ^{20}Na and ^{21}Mg produced in the ^{20}Ne (^{3}He, p2n) and ^{20}Ne (^{3}He, 2n) reactions at a bombarding energy of 40 MeV. The results were in good agreement with the curves given in Fig. 3-11.

Considerations for a solid target system change to some degree with each projectile-target combination because of the differing range-energy behavior of the recoiling compound nuclei. Light ions normally lose relatively little energy in traversing a target which is one recoil length thick making the effective bombarding energy the same throughout, while heavy ions lose much greater amounts of energy in traversing the system (target plus gas) creating a substantial bombarding energy gradient and often a dramatic cross section change. These conditions were empirically optimized by maximizing the number of targets which could be effectively utilized with the choice of an overall 8-12 capillary system. The twelve-capillary, three target system shown in Fig. 3-12 was thus constructed for light ion reactions such as would be needed for the A=4n, $T_z = -2$ series studies of radioactive nuclides. The four capillaries for each target provide

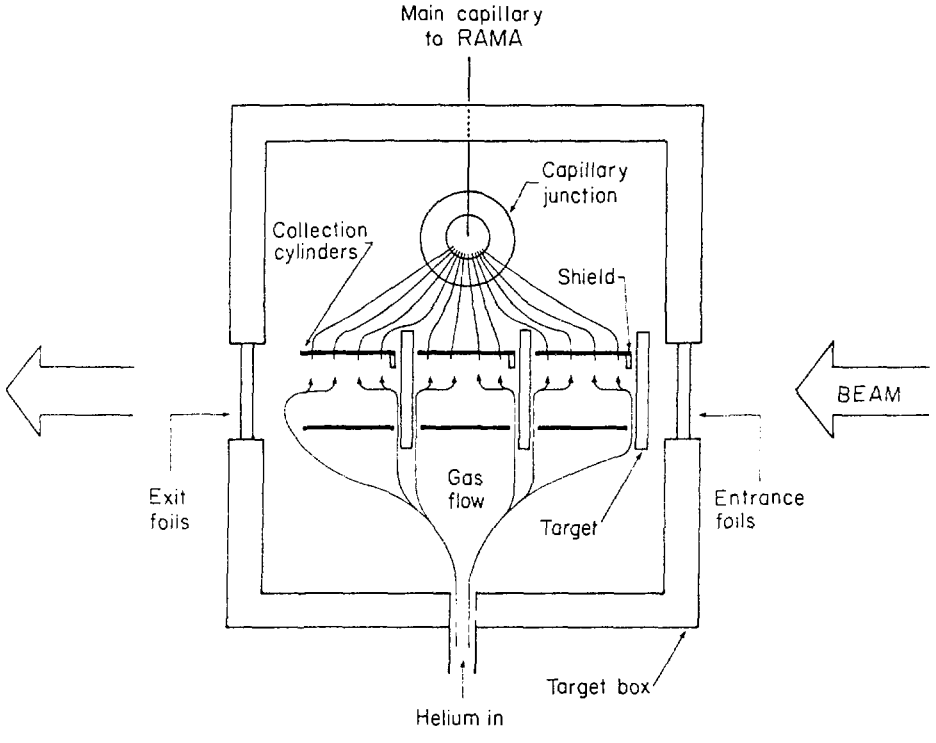

Fig. 3-12. Schematic diagram of the solid target multiple capillary used for light-ion reactions.

collection from approximately one recoil range for compound nuclei formed at the back of a target. This increase in the effective collection volume for each target multipled by the three targets total again yielded approximately a tenfold increase in yield. A second, ten-capillary two-target system was constructed to accomodate target-projectile combinations in which the projectile ranges from ^{10}B to ^{20}Ne. For incoming projectiles heavier than ^{20}Ne, a ten capillary system is used with a single target. The overall transport times for all of these multiple capillary systems have been measured with the 446 ms beta-delayed alpha-particle emitter ^{20}Na by pulsing the cyclotron on for 0.1 s and off for 3s. The observed tranported times for all of these target-capillary combinations are listed in Table 3-3.

As was mentioned in Section 3-A, the opening angle for the heavy clusters needs to be $\leq 2^{o}$ to reach the plasma region of the ion source. Ethylene glycol has traditionally been used as our additive for efficient transport for the RAMA helium-jet because it most effectively met this small opening angle criterion. The results, however, were not as reproducible as might be desired. The transport efficiency at low beam intensity has been observed to depend on the beam current passing through the helium and in a manner scaling approximately as $[dE/dx]^{-1}$ for the different projectiles. The general capability of handling increased beam on target was then necessary to improve the transport efficiency as well as to increase the actual production. Unfortunately for heavier projectiles, the entrance and exit windows burst when too much beam was incident. To allow a nominal beam trebling, double-windowed entrance and exit foil

Table 3-3. Experimental Transport Times for Various Capillary Systems.

Transport Gas	Target System	Main Capillary Diameter (mm)	Transport Time (ms)
1. Helium	Single Capillary	1.0	200
2. S.C. Neon[a]	Gas M. C.[b]	1.0	260
3. Helium	2 Target M. C.[c]	1.0	520
4. Helium	3 Target M. C.[d]	1.0	535
5. Helium	Single	1.4	95
6. S. C. Neon	Gas M. C.	1.4	170
7. Helium	2 Target M. C.	1.4	180
8. Helium	3 Target M. C.	1.4	200

S. C. Spark Chamber, M. C. Multiple Capillary

[a] S. C. Neon ≡ .9 Ne + .1 He

[b] Gas M. C. ≡ 12 x 1.0 mm

[c] 2 Target M. C. ≡ 5 x 1.0 mm each

[d] 3 Target M. C. ≡ 4 x 1.0 mm each

systems were incorporated (see Fig. 3-9), in which cold nitrogen gas is directed onto the windows. This process naturally cooled the helium-jet region to temperatures near or below $0^{o}C$. This cooling effect reduced the ethylene glycol concentration in the bombardment region, nevertheless it was observed that the opening angle had been reduced (i.e., the cluster size had apparently increased). Monitoring the gas temperature and the temperature of the collection cylinder led to implementing independent cooling of the collection cylinder because if T_{cyl} and T_{gas} differed greatly, a total extinction of yield was noted. The optimum gas temperature for $^{3}He^{+2}$ induced reactions has been found to be $-7\pm10^{o}C$, and the cylinder temperature is maintained within ten degrees of this value. Additional helium-jet information may be found in Appendix A.

2. Ion Source Region

Two major goals in the redesign of the ion source were to decrease the distance between the capillary exit and the plasma region and to raise the acceleration potential to 18 kV (from the 11 kV limit established earlier by the existing high voltage insulators). Given the design criterion that the critical internal dimensions of our hollow-cathode ion source must remain intact, a modified ion source and its holder as shown in Fig. 3-15 were designed. This new ion source is only 9 cm long, as compared with ~21 cm for the original. Elimination of the focusing solenoid which was found to be ineffective produced a higher geometry and provided better vacuum pumping in the extraction region, thereby reducing scattering between the ions and

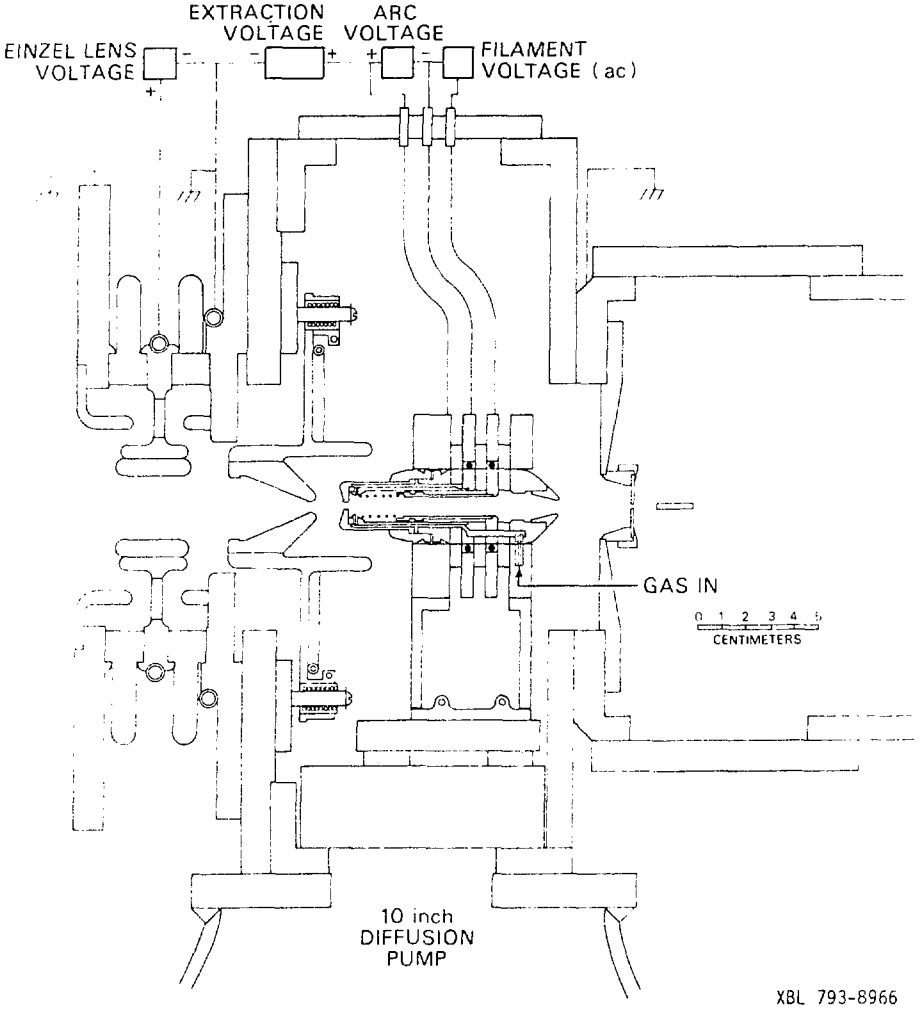

Fig. 3-13. Schematic diagram of the new RAMA ion source region.

spectator neutral molecules (or atoms). The extractor and Einzel lens assemblies of the original RAMA design were left unchanged.

Tests with internally produced 18 keV beams of $^{40}Ar^{+}$ and $^{20}Ne^{+}$ showed that the system could be operated for long periods of time with no apparent changes in beam characteristics. It was determined that the Einzel lens could be operated at a significantly lower potential (12-13 kV) than the 18 kV extraction potential in con- trast to results at 10.5 kV (in which the Einzel lens voltage was required to be approximately .9 of the extraction voltage). As an example of the resolution obtainable with this improved ion source, a channeltron electron multiplier (CEM) scan of the stable tin isotopes between masses 114 and 122 is shown in Fig. 3-14. The observed resolution at full-width one-tenth maximum has increased to 304 (from 194). Since all of the optical parameters were found to scale by either

$$\sqrt{\frac{E_F}{E_I}} \qquad \left(\sqrt{\frac{18}{10.5}} = 1.31\right)$$

for magnetic elements or $\frac{E_F}{E_I}$ (1.71) for electrostatic elements (see Appendix C), this increase in resolution can be attributed to a lowered ion source emittance, the reduced pressure in the extractor region, and the reduced space charge effects at this beam energy.

Tests with radioactivity were also performed to determine the effects of these changes on the actual throughput of the ion source. The effects of increasing the extraction potential from 10.5 to 18 kV were checked with the rare-earth alpha-particle emitter ^{153}Er produced in the $^{142}Nd(^{16}O,5n)$ reaction at 105 MeV; this effect was

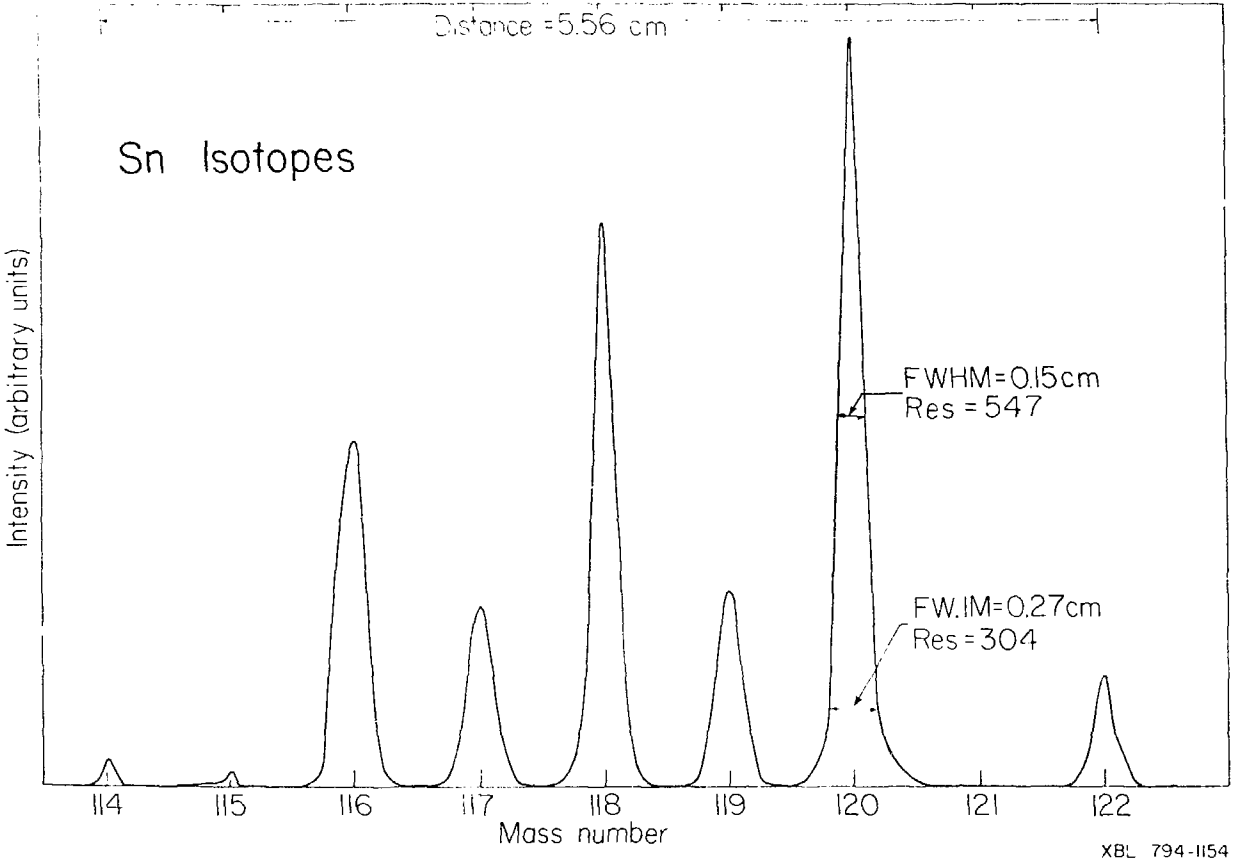

Fig. 3-14. Channeltron electron multiplier scan of stable tin isotope from mass 114 to 122 at 18 kV.

observed to be a factor of five. The total yield for ^{153}Er increased by a factor of ten, implying that shortening the ion source gave a factor of two. This factor of ten increase in yield for erbium has been found to hold true for many elements. Table 3-4 lists typical efficiencies for some examples of activities with vastly differing chemical properties. Except for sodium, the typical overall efficiency for RAMA is now ~0.1%. Additional information concerning ion source operation may be found in Appendix B.

Extensive tests performed with the beta-delayed alpha-particle emitter ^{20}Na produced at 40 MeV by the $^{20}Ne(^{3}He,p2n)$ reaction showed that the efficiency for sodium had increased a factor of approximately one hundred, rather than the factor of ten noted above. This can be accounted for as follows. Most of the plasma surroundings are at the cathode potential and the plasma is near the anode potential, making acceleration of positive ions from most of the surroundings into the plasma impossible. Any species, however, collected on the anode cap which could easily be surface ionized could reenter the plasma for extraction, and it is this effect which is probably the source of the additional sodium yield. Later tests with cesium activity gave even larger increases in yield, which in consideration of the even easier surface ionization of cesium reinforces this conclusion.

Table 3-4. RAMA Efficiencies

	^{20}Na	^{21}Mg	^{153}Er	^{25}Si
He-Jet	70%	26%[a]	50%	32%[a]
Skimmer	70%	70%	70%	70%
Ion Source and Magnetic Analysis	2.0%	0.45%	0.4%	0.5%
Overall	1.0%	0.08%	0.12%	0.11%

a) Includes loss due to short half-life and a nominal 70% efficiency.

3. Detection System Improvements

Due to the expected low yeilds on the RAMA focal plane for many of the reaction products of interest, high solid angle detector systems are a necessity in increasing the overall efficiency. A high solid angle system for charged particle detection (incorporating two detector telescopes for reasons noted below) was developed as shown in Fig. 3-15; this system possesses a det ction efficiency of 38% of 4π for higher energy particles. The o_iginal telescope used 300$\mu g/cm^2$ Kimfoil catcher foils rather than the carbon foils shown. These thick Kimfoils proved to degrade the energy of the protons (observed in beta-delayed proton decay) and thus limit the measured peak width. The present system with 2 x 25 $\mu g/cm^2$ carbon foils was subsequently incorporated. A standard electronics setup used with these telescopes is shown schematically in Fig. 3-16.

A method to measure the half-life of very short-lived nuclides (<200ms) was also needed, but any mechanical device to move the activity is general fairly slow. Even the flipper wheels discussed in Section 3-D with the ~40 ms flip times could not be operated on a 200 ms timescale without consistent mechanical failure due to the violent nature of such a rotation. However, introducing the double stack of telescopes shown in Fig. 3-15 and the capability of fast vertical switching of the beam permits two collection counting cycles while losing almost no data. The RAMA beam can be flipped from an "up" to a "down" position by reversing the polarity on the vertical deflection

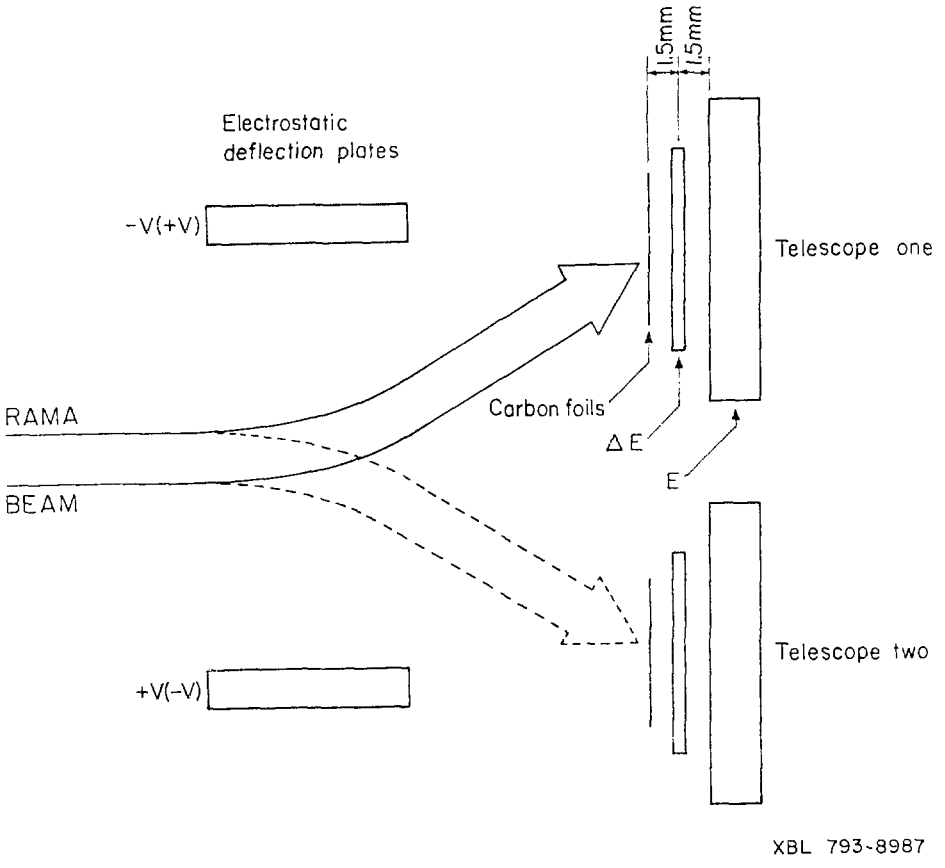

Fig. 3-15. Schematic diagram of the solid-state particle detector telescope used for measuring the decay properties of short-lived particle emitters. Changing the beam from the "up" to the "down" position on a cyclical basis permits half-life determinations.

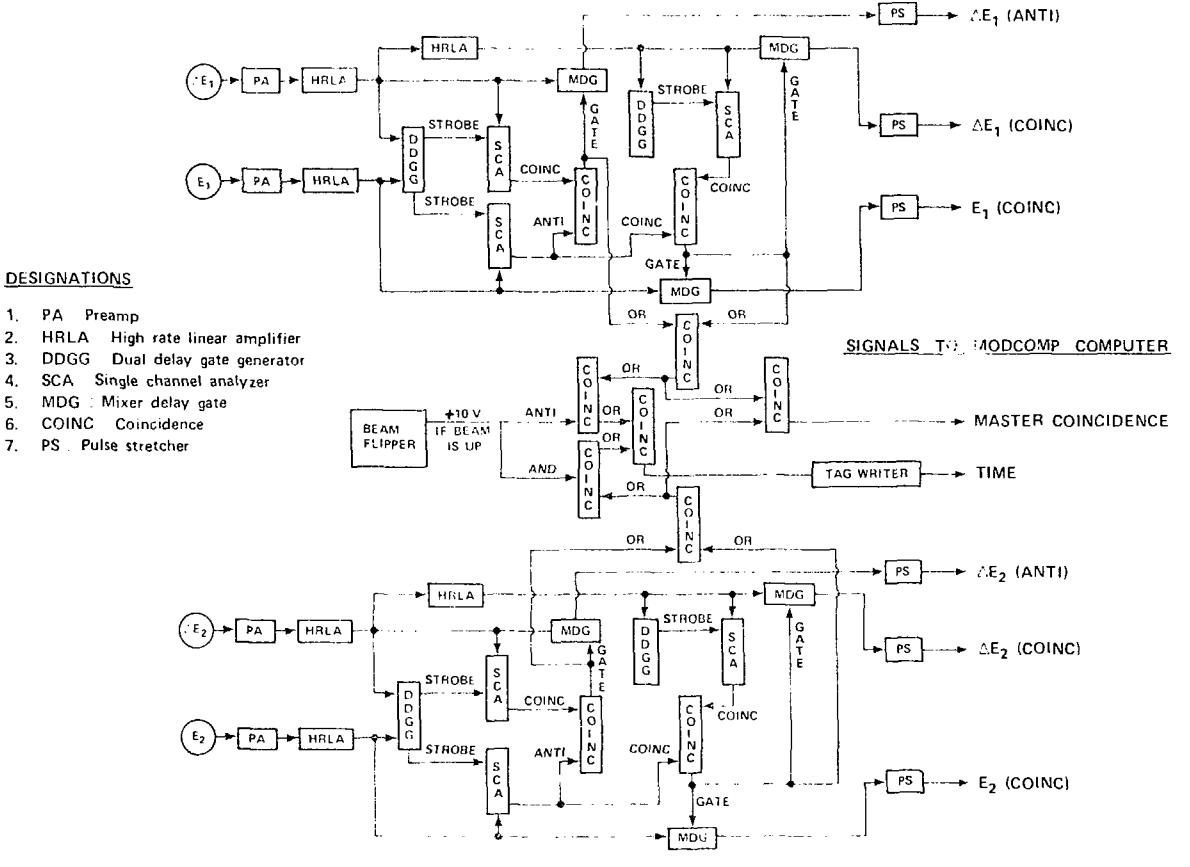

Fig. 3-16. Schematic diagram of electronics setup used with double-stacked detector telescopes.

XBL 796-1874

plates shown in Fig. 3-9. This polarity change is accomplished by a fast driven vacuum tube system which has been tested at a 100 μs cycle time even though nominal flip sequences are on the order of 200 ms. Since the resultant deflection on the focal plane is ±2 cm from the central plane, this deflection does not seriously affect the optical properties. The technique was checked by remeasuring the half-life of ^{20}Na. The observed value of 446 ms agrees well with previous results.

IV. EXPERIMENTAL RESULTS

A. ^{20}Mg Decay

Detection of the decay of ^{20}Mg established the location of the lowest T = 2 state in ^{20}Na, thereby completing the second known isospin quintet (Ro 76) but the first in which all members of the multiplet are bound to isospin-allowed particle decay modes. ^{20}Mg also represents the lightest nucleon-stable member of this A = 4n, T_z = -2 series of beta-delayed proton emitters even though the rare gas ^{32}Ar has been previously characterized (Ha 77b). Completion of the mass twenty quintet thus represents an effective test for a possible deviation from the quadratic isobaric multiplet mass equation (IMME) as discussed in Section II:

$$M(A,T,T_z) = a(A,T) + b(A,T)T_z + C(A,T)T_z^2 \qquad (4\text{-}1)$$

where the coefficients a, b, and c are related to diagonal reduced matrix elements of the charge dependent part of the nuclear Hamiltonian. As noted earlier, deviations from the quadratic form are generally represented by additional terms $d(A,T)T_z^3$ and $e(A,T)T_z^4$ whose coefficients are related to off-diagonal matrix elements and can be derived from second-order perturbation theory.

Beams of 70 MeV $^3He^{+2}$ ions from the 88-inch cyclotron of intensity 2-7 μA were used to produce ^{20}Mg nuclei via the ^{20}Ne (^{3}He,3n) reaction. A schematic diagram of the cyclotron and beam transport system is shown in Fig. 4-1. The target employed was spark chamber gas (90% Ne and 10% He), which for these experiments

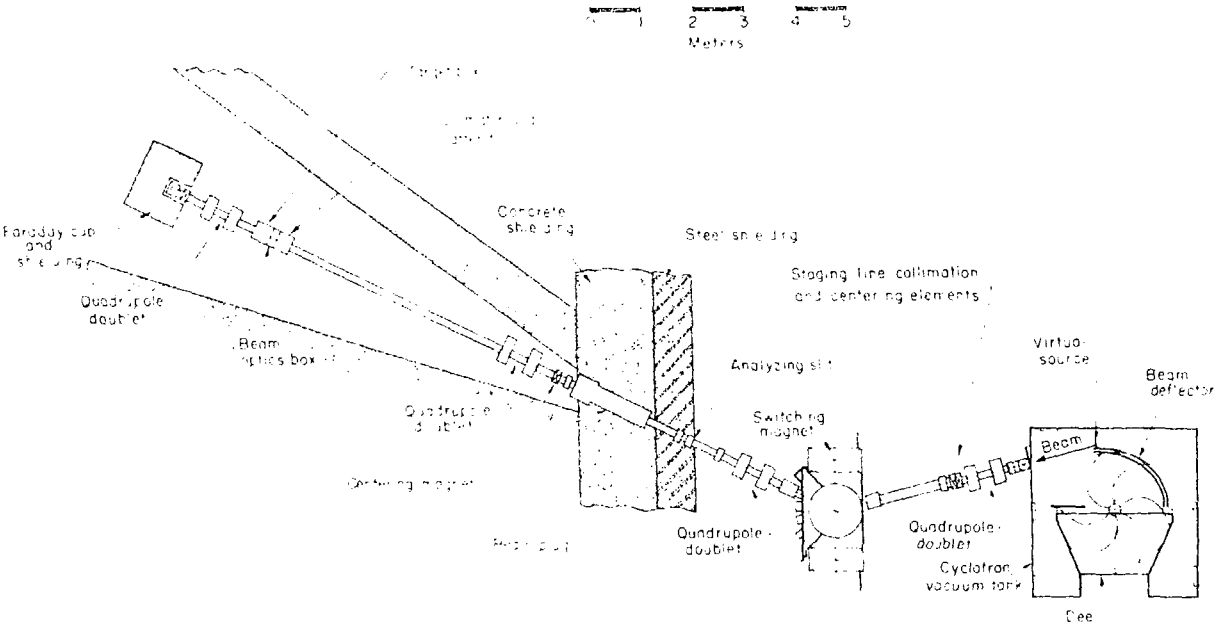

Fig. 4-1. Schematic diagram of the 88-inch cyclotron, beam transport system, and the Cave 2 experimental area. The target box shown here is the RAMA target box shown in Fig. 1-1.

necessarily served as the stopping and the transport medium. A more complete description of the beam transport facilities may be found elsewhere (Vi 78). The details of the helium-jet transport and mass separation are given in Chapter III in addition to details on the detection system utilized. The vertical detection unit was pulsed on a 200 ms timescale in accordance with the production of ^{21}Mg half-life of ~100 ms.

Having $J^{\pi} = 0^{+}$ and T = 2, ^{21}Mg is expected to undergo superallowed β^{+} decay to the 0^{+} (T = 2) analog state in ^{21}Na in addition to strong allowed transitions to lower-lying $T = 1$ states (Da 75). The quadratic IMME prediction and the β-delayed proton data in ^{20}Na lead one to expect ~4.1 MeV energy for the proton transition from the analog state in ^{20}Na to the ground state of ^{19}Ne (Ma 77, Ar 76b). Calibration of the solid state detector telescope pair was accomplished by detecting the well-known ~500 ms two-delayed proton emitter ^{22}Mg, produced in much higher yield in the $^{20}Ne(^{3}He,2n)$ reaction. A proton spectrum arising from the decay of 122 ms ^{21}Mg is shown in Fig. 4-2 a); the 1.637 and 3.669 MeV provided convenient calibration points.

The proton spectrum arising in the decay of ^{21}Mg after bombardment for 700 mC is shown in Fig. 4-2 b). Two distinct proton peaks are evident with weighted average energies from four separate measurements giving 4.16±.05 and 3.95±.09 MeV. The number of counts in these two peaks yield an observable cross section of [illegible]. A half-life of 95^{+60}_{-30} ms was observed for these peaks. Substantial contamination problems were encountered at the mass twenty position due to [illegible]

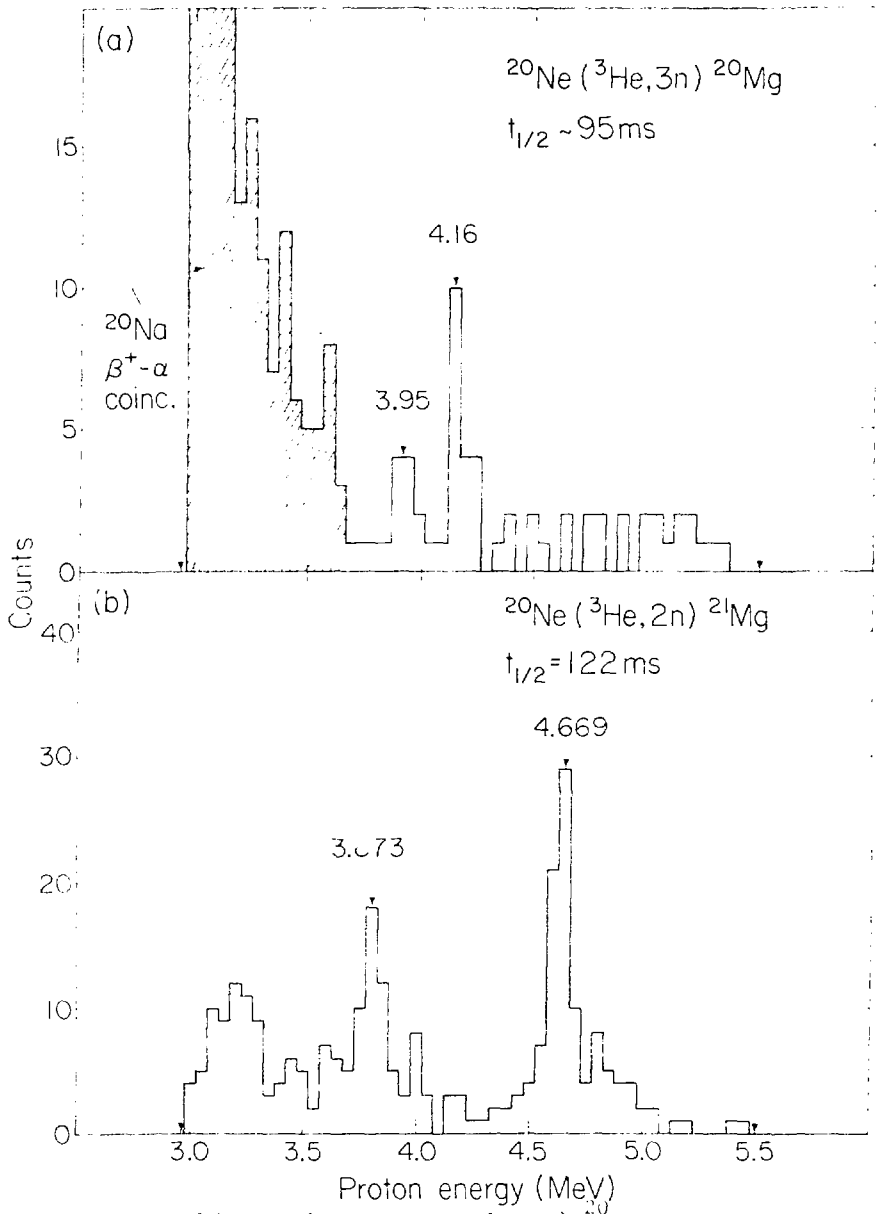

Fig. 4-2. Spectra of beta-delayed protons from a) ^{20}Mg and b) ^{21}Mg. Both spectra are a combination of three separate runs. Arrows at low and high energy indicate telescope cutoffs. The high detection efficiency results in "sum" peaks due to simultaneous detection of a proton with its preceding positron. The broad peak ~200 KeV above the 4.669 group represents such a peak.

XBL 7810-11653

intense ^{20}Ne beam from the target gas and to very high "background" from the strong β^+-delayed alpha-particle emitter ^{20}Na ($t_{1/2}$ = 446 ms). ^{20}Na was copiously produced in the competing ^{20}Ne (^{3}He,p2n) reaction with resultant activities on the focal plane in the ratio of (~10^5) ^{20}Na 2.16 MeV alpha- particles per (1) ^{20}Mg proton. Even utilizing standard particle identification techniques (Go 64), complete removal of ^{20}Na activity was not possible due to real coincidences between positrons in the E counter of the telescopes and alpha-particles of reduced energy due to the foils (~1.0-1.5 MeV) in the ΔE counters. Those events in the cross-hatched region at lower energies of the ^{20}Mg spectrum in fact possess the ^{20}Na half-life. It should be noted that the two peaks attributed to the decay of ^{20}Mg can not arise from the possible beta-delayed proton decay of ^{20}Na since the maximum proton energy available in ^{20}Na decay is 0.99 MeV.

The 4.16 and 3.95 MeV proton groups in Fig. 4-3(a) can be attributed to the isospin-forbidden proton decay of the lowest 0^+, T = 2 state in ^{20}Na. This ^{20}Na state is fed via a pure Fermi (superallowed) transition ($0^+ \rightarrow 0^+$, T = 2) with a calculated log ft of 3.18. The measured half-life combined with the calculated log ft value yields a branching ratio of 3±2% for the superallowed transition. A proposed partial decay scheme for ^{20}Mg is shown in Fig. 4-3. The measured proton energy in the center of mass taken together with the ^{19}Ne mass excess (Wa 77) yields a mass excess of 13.42±.05 MeV for the lowest 0^+(T = 2) state in ^{20}Na.

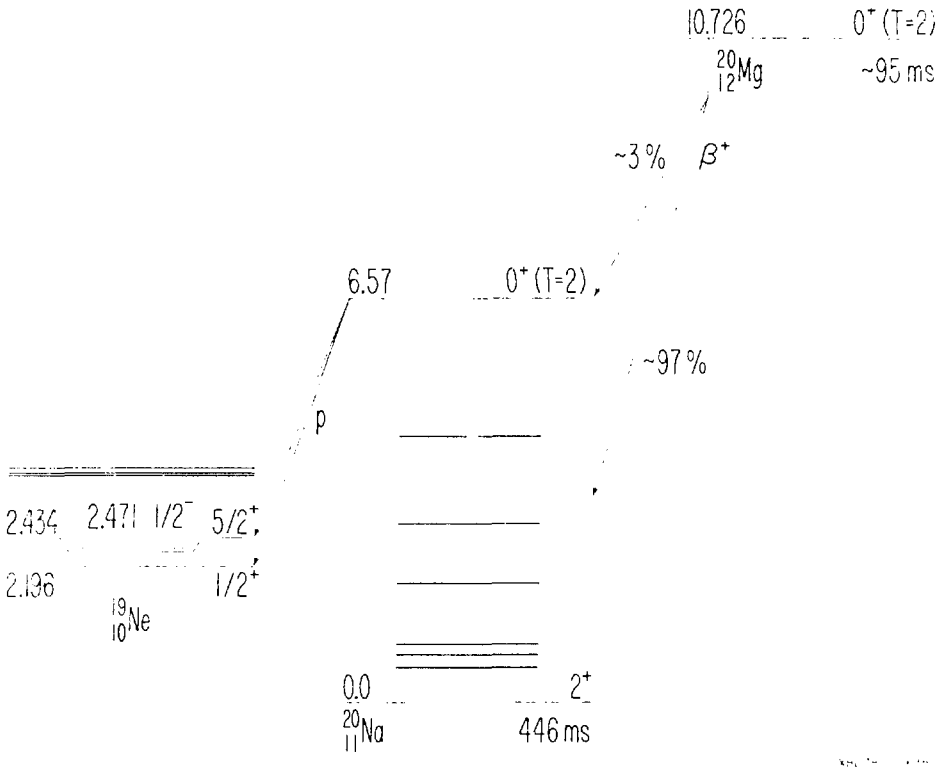

Fig. 4-3. Proposed decay scheme for ^{20}Mg.

B. ^{24}Si Decay

After the characterization of the decay of ^{20}Mg, the next member of the A = 4n, T_z = -2 series of beta-delayed proton emitters to be studied was ^{24}Si. Unlike mass twenty, the determination of the 0^+, T = 2 state in ^{24}Al does not, however, complete the quintet because an accurate mass for ^{24}Si has not yet been determined. Again beams of 70 MeV $^3He^{+2}$ ions of intensity 3-5 A were used to produce ^{24}Si via the ^{24}Mg (^{3}He,3n) reaction. The three-target multiple capillary system (see Chapter III) was used in conjunction with three, 1.2 mg/cm^2 Mg targets to optimize the yield of the low cross section and short-lived ^{24}Si.

The mass separated ion beams of interest were implanted on a ~50 μg/cm^2 carbon foil which replaced the thick aluminized polycarbonate collection foils used in the ^{20}Mg experiments. The remainder of the telescope geometry remained identical with the minimal observable energy being approximately 1.5 MeV, even though the detection efficiency decreased for protons of energy less than ~3.0 MeV.

Since ^{24}Si also has $J^\pi = 0^+$ and T = 2, it is expected to undergo superallowed β^+ decay to the 0^+(T = 2) analog state in ^{24}Al in addition to strong allowed transitions to lower-lying 1^+ states, predicted by shell model calculations (Ro 73). The quadratic IMME prediction and the proton binding energy in ^{24}Al lead one to expect ~3.9 MeV laboratory energy for the proton transition from the analog state to the ground state of ^{23}Mg. Calibration of the detector telescope was accomplished by detecting the well-known

beta-delayed proton emitter ^{25}Si (Se 73b), produced in much higher yield in the ^{24}Mg (^{3}He,2n) reaction.

A proton spectrum arising from the decay of 220 ms ^{25}Si is shown in Fig. 4-4(b); the groups at 4089±2 keV and 5403±2 keV provided convenient calibration points. These calibration energies were derived from the most recent value of the excitation energy of the lowest T = 3/2 state in ^{25}Al (Ro 77c). Events in the shaded areas in both spectra are due to the simultaneous detection of a proton and its preceding positron in this large solid angle telescope.

The proton spectrum arising from the decay of ^{24}Si after bombardment for 560 mC is shown in Fig. 4-4(a). Only one peak is evident in the spectrum; it occurs at a laboratory energy of 3.914±0.009 MeV. Possible lower energy groups arising from positron decay to 1^{+} states were not observed, a result partly due to the low detection efficiency of the detector telescope below 3.0 MeV. The background appears to arise from (n,p) reactions on silicon in the E detector which pass through the ΔE detector. The particle identification spectrum for these enevents covers a range encompassing low energy electrons (or positrons) and high energy protons making complete elimination of such events impossible. A half-life of 100^{+90}_{-40} ms was estimated for the observed peak by comparing the ^{24}Si focal plane yield to the yields of ^{20}Na ($t_{1/2}$ = 446 ms), ^{24}Al (2.07s), ^{24m}Al (129 ms), and ^{25}Si (220 ms). Relative cross sections for these nuclides were estimated by using the OVERLAID ALICE code (Bl 76) as well as by the experimental cross section values for the ^{20}Ne-^{21}Ne case. The observed cross section for ^{24}Si was

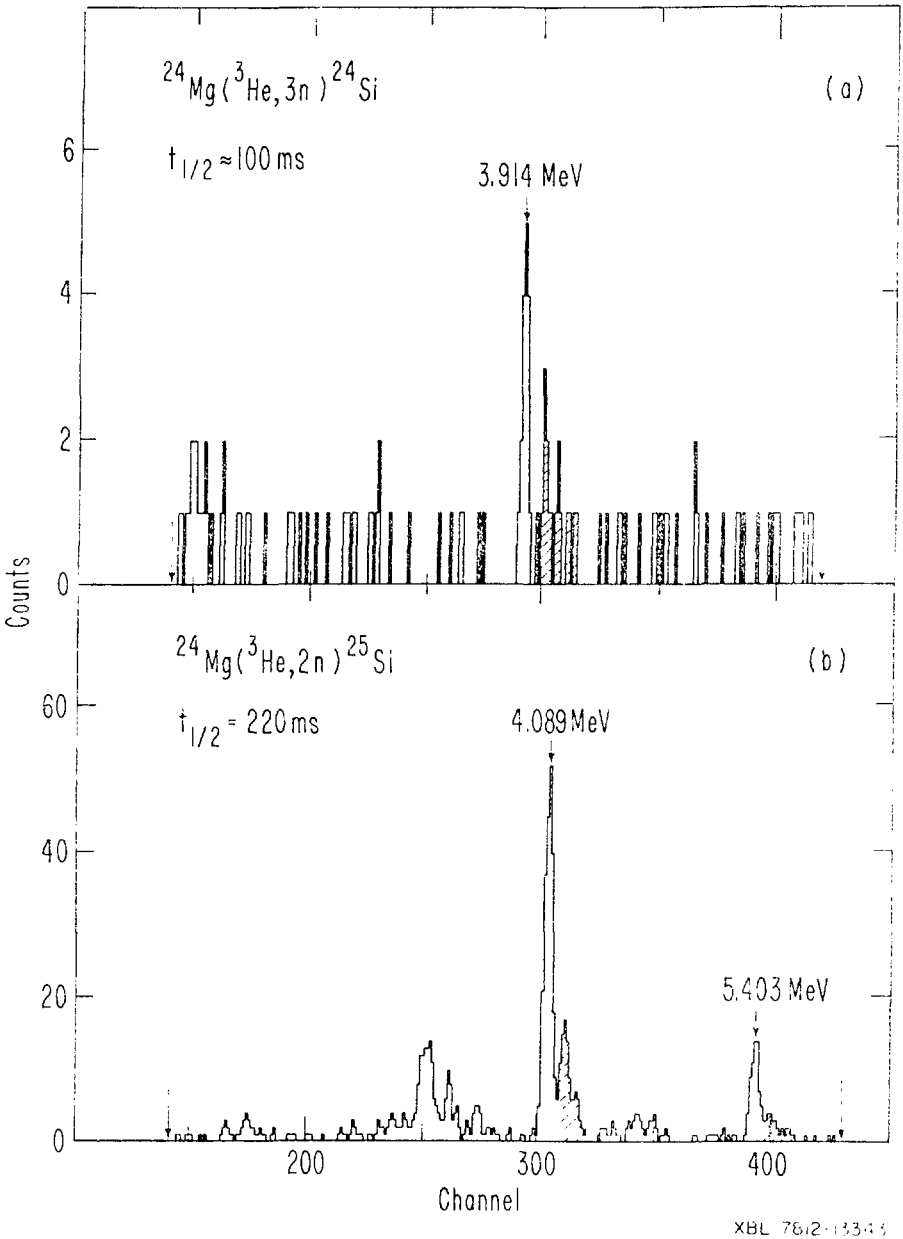

Fig. 4-4. Spectra of beta-delayed protons from a) ^{24}Si and b) ^{25}Si. Arrows and shaded areas are as in Fig. 4-3.

~2 μb compared with 150 μb for ^{25}Si (Es 71). The weak beta-delayed alpha-particle emitter ^{24}Al (Ho 79 and En 73) also served as a very convenient monitor during the ^{24}Si experiment. A spectrum of these delayed alpha-particles is shown in Fig. 4-5. It should be noted that the peak attributed to the decay of ^{24}Si can not arise from the possible beta-delayed proton decay of ^{24}Al or ^{24m}Al, since the maximum available proton energies in these latter decays are 2.1 and 2.4 MeV, respectively.

The proposed decay scheme for ^{24}Si is shown in Fig. 4-6, in which the 3.914 MeV proton group is attributed to the isospin-forbidden proton decay of the lowest 0^+, T = 2 state in ^{24}Al. Since the superallowed transition to this ^{24}Al state has a calculated log ft of 3.18, allowed beta decay to other states near this excitation energy of 5.955 MeV would lead to considerably lower intensities in the proton spectrum. Taking the center of mass proton energy together with the ^{23}Mg mass excess (Wa 77), one obtains a mass excess of 5.903±0.009 MeV for the 0^+(T = 2) analog state in ^{24}Al. Since the ^{24}Si ground state mass has not yet been measured, a mass excess of 10.75±0.16 Mev was predicted using the quadratic IMME. The decay energy and estimated half-life combined with the calculated log ft-value yield a branching ratio of 7^{+6}_{-4}% for the super-allowed beta transition.

C. IMME Comparisons

These mass measurements represent different degrees of tests for the isobaric multiplet mass equation since the mass 20 quintet is now complete but the mass 24 quintet still lacks the mass of ^{24}Si. The

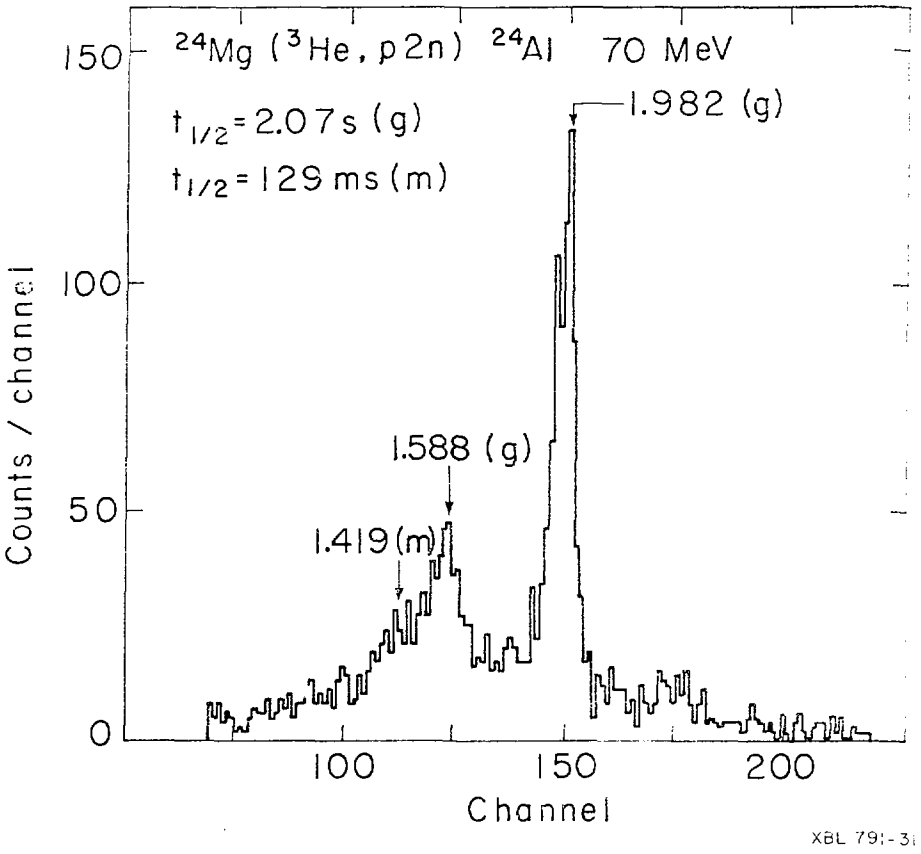

Fig. 4-5. ΔE singles spectrum obtained simultaneously with the ^{24}Si spectrum in Fig. 4-5a showing the delayed alpha-particles from ^{24}Al.

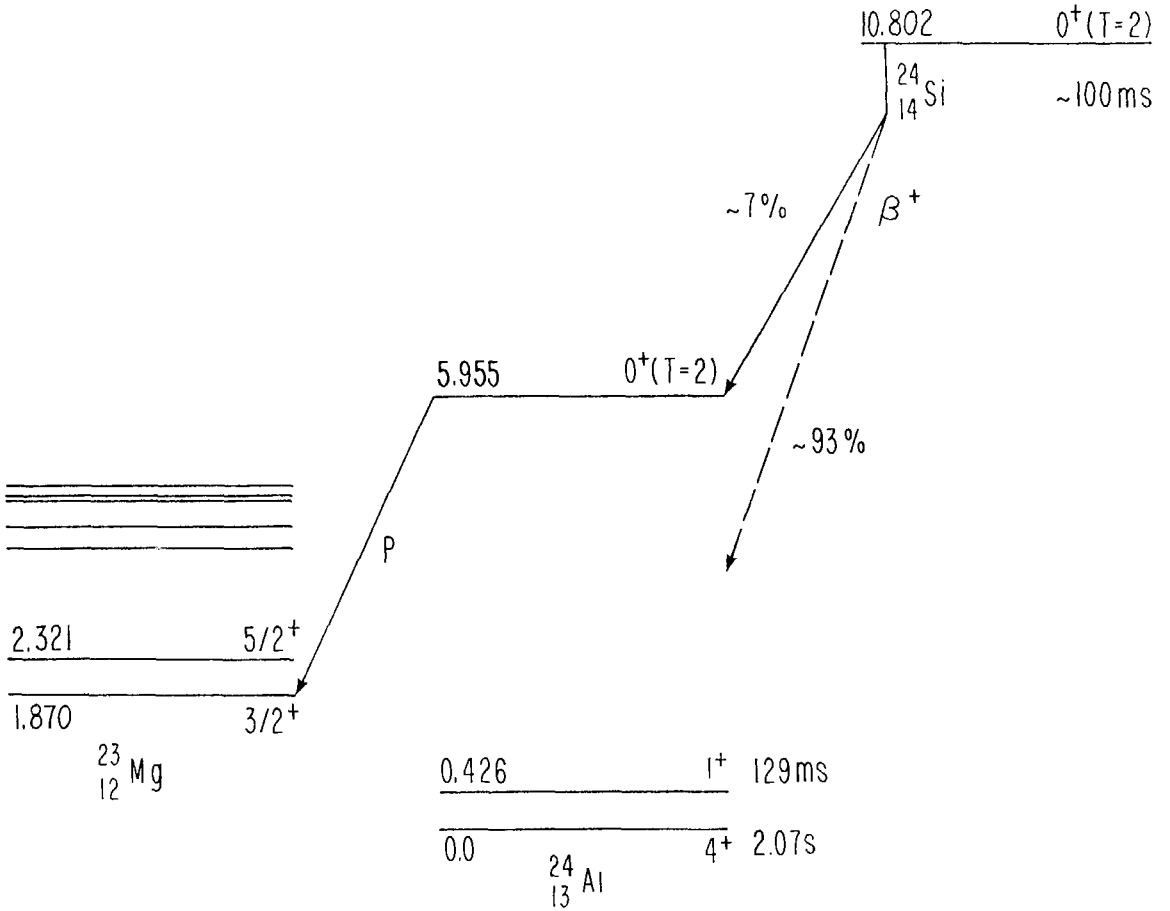

XBL 7812-13344

Fig. 4-6. Proposed decay scheme for ^{24}Si. The ^{24}Si-^{24}Al mass difference is taken from the quadratic IMME prediction.

mass values for all of the mass twenty isospin quintet are given in Table 4-1 (Bl 67, Ku 67, Ad 69, and Mi 76). When these are used to test the IMME whose coefficients also appear in Table 4-1, an excellent fit (normalized χ^2 0.98) is obtained by using only the quadratic form, reflecting the insignificance of charge dependent mixing in the mass twenty multiplet. This contrasts with the results from the only other complete quintet (A=8) which clearly indicates a non-quadratic form for the IMME (Ro 75, Ro 76, and Tr 76a). This deviation has been discussed in terms of the strong Coulomb repulsion associated with the particle-unbound members in this quintet, in addition to the effect of isospin mixing in the $T_z = 0$ member of this multiplet (Ro 75 and Ro 76). On the other hand, in the A = 20 quintet, all members are stable toward isospin-allowed particle decay. As noted in Section II, major isospin mixing would be expected to show up in the e-coefficient; however, any observation of a non-zero quartic term would require much more accurate measurements of the masses of most of the members in the multiplet. These results on the mass twenty quintet with its narrow states, then, are in accord with all but one of the numerous measurements on isospin quartets (Be 79) in showing excellent agreement with the simple quadratic mass equation and no evidence for substantial charge dependent effects.

The A = 24 isospin quintet is not complete since the ground state mass of ^{24}Si has not yet been measured. The experimental mass values for the four known members of this quintet are given in Table 4-2 (St 63, Ri 67, Os 78, and Mc 78). In addition, calculations with a cubic form for this mass equation are presented. Both sets of

Table 4-1. Properties of the A=20 isobaric quintet and coefficients of the IMME[a].

Nucleus	T_z	Mass Excess M (MeV)	E_x (MeV)	Reference
^{20}Mg	-2	17.57 (3)	0.0	(Tr 76b)
^{20}Na	-1	13.42 (5)	6.57 (5)	this work
^{20}Ne	0	9.6908 (23)	16.7325 (23)	(Bl 67, Ku 67 Ad 69)
^{20}F	1	6.503 (3)	6.519 (3)	(Mi 76)
^{20}O	2	3.799 (8)	0.0	(Wa 77)

Predicted coefficients (MeV) for the IMME[a]: $M(T_z)=a+bT_z+cT_z^2+dT_z^3+eT_z^4$

a	b	c	d	e	χ^2
9.6917 (22)	-3.4372 (51)	0.2466 (33)	0	0	.98
9.6909 (23)	-3.4347 (56)	0.2489 (39)	0.0022 (20)	0	.71
9.6908 (23)	-3.4440 (74)	0.2588 (101)	0	-0.0025 (19)	.33
9.6908 (23)	-3.463 (34)	0.278 (34)	0.005 (9)	-0.007 (9)	-

a) The numbers in parentheses for the masses and the mass equation coefficients represent the uncertainties in the least significant figures.

Table 4-2 Properties of the A=24 isobaric quintet and coefficients of the IMME.

Nucleus	T_z	Mass Excess M (MeV)	E_x (MeV)	Reference
^{24}Si	-2	10.750 (16)	0	IMME-Prediction (quadratic)
^{24}Al	-1	5.903 (9)	5.955 (10)	This work
^{24}Mg	0	1.5016 (16)	15.432 (2)	(Ri 67, Os 78, Mc 78)*
^{24}Na	1	-2.4473 (12)	5.9702 (9)	(St 73)
^{24}Ne	2	-5.949 (10)	0	(Wa 77)

Predicted coefficients for the IMME: $M = a+bT_z+cT_z^2+dT_z^3$

a	b	c	d	χ^2
1.5018 (15)	-4.1742 (37)	0.2250 (34)	-	0.13
1.5016 (16)	-4.1743 (37)	0.2263 (48)	-0.0009 (25)	-

*The quoted value is the weighted mean of the results given in the references.

IMME coefficients show clearly the insignificance of the cubic term. The value of a possible d-coefficient, -0.9±2.5 keV, is consistent with zero, reflecting the absence of higher order charge dependent effects. The small $\chi^2 = 0.13$ arises because all of the A = 24 masses lie on the same line. (A more complete description of the error analysis may be found in Appendix D). This result is in good agreement with representative 4n+1 quartet and all 4n quintet data except mass 8 as noted earlier.

A comparison of some of the IMME d-coefficients in which four or more members of an isospin multiplet are known for both the A = 4n quintet series and the A = 4n+1 quartet series is made in Table 4-3. Only the mass 8 and mass 9 systems exhibit substantial deviations; these have already been described by Coulomb repulsion associated with particle unbound members nd isospin mixing effects. Figure 4-7 is a graphical representation of the d and e coefficients for isospin quintets with four or more known members.

Since isospin quintets with A = 24, 32, and 36 now have four known members each, accurate measurements of the fifth members of the multiplets, although a difficult experimental task, would clearly be of substantial value. Accurate half-lives of all of these $T_z = -2$ nuclei would also be useful to further check the absolute log $\underline{ft}$ values associated with these $0^+ \rightarrow 0^+$, T = 2 pure Fermi decays. Current statistics are wholly inadequate for this purpose, though, and would require either very long experiments or substantial RAMA efficiency increases.

Table 4-3. Comparison of IMME d-coefficients for some A=4n+1 and A=4n Nuclei.

T_z = -3/2 Nuclei	IMME - d-coefficient	Reference
^{9}C	5.8±1.6	(Ka 75)
^{13}O	-0.5±2.3	(Ke 78, Ha 71)
^{17}Ne	4.8±5.6	(Ke 78, Es 70)
^{21}Mg	3±5	(Se 73a)
^{25}Si	2±3	(Se 73b)
T_z = -2 Nuclei		
^{8}C #	5.6±2.2	(Ro 75, Ro 76, Tr 76a)
^{12}O #*	0±11	(Ke 78)
^{16}Ne#*	8±5	(Ke 78)
^{20}Mg	-2.2±2.0	This work
^{24}Si *M	-0.9±2.5	This work
^{32}Ar *M	0.5±2.5	(Ha 77b)
^{36}Ca *	-1.6±1.8	(Tr 77)

= Unbound member

* = Incomplete quintet

M = Unmeasured mass of T_z = -2 member of multiplet

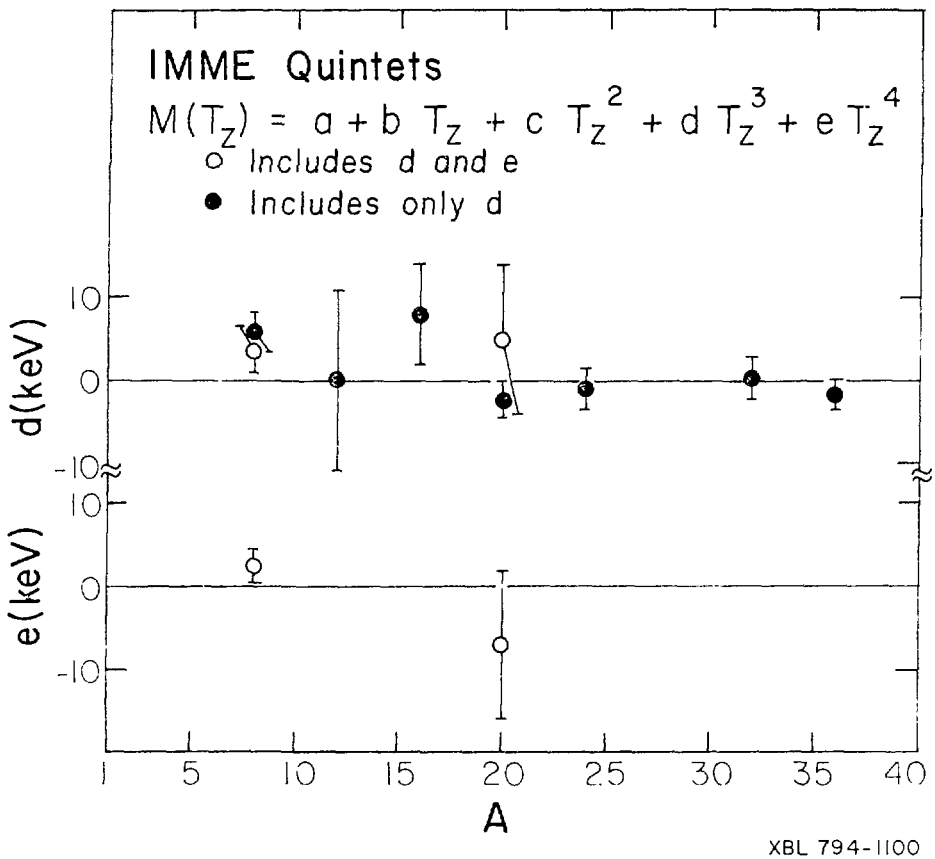

Fig. 4-7. Graphical representation of IMME d and e coefficients for both completed isospin quintets (light circles) and for isospin quintets where only four members are considered (dark circles).

V. CONCLUSIONS

It has been demonstrated that RAMA is generally chemically universal. If the ion source temperature is significantly above the melting point to eliminate vacuum pumping of the species of interest, the efficiency for most of the elements is approximately constant except for the alkali metals; the higher efficiency for these metals can probably be explained by the easy surface ionization of these species. Table 5-1 lists the elements observed on the RAMA focal plane as activity. This list shows the great versatility of RAMA but is by no means exhaustive. Present ion source techniques should permit observation of ~75 of the known elements. Small improvements in ion source technology should expand this capability to include 90 of the known elements.

Detection of the beta-delayed protons from the decays of two members of the A=4n, $T_z = -2$ series, ^{20}Mg and ^{24}Si, establish RAMA as an effective instrument for studying activities with observable cross-sections of 1 μb and half-lives of 100 ms. This cross section limit is only for experiments involving discrete energy charged particle decay, whereas gamma or beta experiments with current efficiencies would require production cross-sections of ~500 μb.

Measurements of the masses of the lowest T=2 (0^+) states in both ^{20}Na and ^{24}Al constitute major tests of the isobaric multiplet mass equation. These results are consistent with the quadratic form of the IMME and indicate that completion of the mass 24 quintet (which lacks the mass of ^{24}Si) and the mass 36 quintet (which lacks the 0^+ (T=2) state in ^{36}K) would be quite useful, since these two

Table 5-1. List of Radioactivities Extracted from the RAMA Ion Source.

1. Na^+	11. I^+
2. Mg^+	12. Cs^+
3. Si^+	13. Ba^+
4. Al^+	14. Tb^+
5. P^+	15. Dy^+
6. K^+	16. Ho^+
7. In^+	17. Er^+
8. Sn^+	18. Tm^+
9. Sb^+	19. Yb^+
10. Te^+	20. At^+

quintets should be easily completed (based on target considerations). Observation of the decay of ^{36}Ca would also serve as a necessary prelude to the possible discovery of the first particle stable $T_z = -5/2$ nuclide, ^{35}Ca. Present statistics on the decays of the $A=4n$, $T_z = -2$ nuclides are insufficient to permit comparisons of absolute log ft values as outlined in Section II. This information would clearly be valuable in further clarifying Cabbibo universality in its relation to high energy physics.

ACKNOWLEDGEMENTS

I wish to express my thanks and appreciation to many people who have helped me during my tenure as a graduate student.

To Professor Joseph Cerny, my research advisor for his inspiration and patience during the many trying hours associated with RAMA's infancy and my inexperience.

To Dr. Rick Gough and Dr. Mike Zisman for guidance during the early years and for critical review of subsequent publications.

To all the postdoctoral fellows, visiting staff members, and Building 88 staff who were supportive of the RAMA project and aided me in learning the rudiments of good nuclear research, Dr. Juha Äystö, Dr. Ralph von Dincklage, Dr. David Scott, Dr. David Hendrie, Dr. Home-Conzett, Dr. Rainer Jahn, Dr. Gary Kekelis, Dr. Howard Wieman, Dr. Hugh Evans from Queen's University, and Dr. Peter Haustein from BNL.

To fellow graduate students both past and present for their experimental assistance and inspiring BS sessions, Ken Wilcox, Bob Weisenmiller, David Vieira, Dieter Stahel, Roger Parry, Jan Wouters, Alden Bice, and Mike Cable.

To all the 88-Inch Cyclotron crew for high quality beams and to all the shop personnel for high quality material workmanship. Special thanks go to Roy Burton for his excellent engineering and designs, to Jack Walton for building the strange detector configurations requested, to Matt Renkas and Don Lundgren for enduring many shenanigans, to Creve Maples for providing many useful computer programs, and to Carol Adams for enduring my handwriting.

To many bridge partners and fellow hellraisers for many evenings of inspiration. Special thanks go to all of the many basketball players I have associated with over the years.

And finally, to all the brewers, vintners, and distillers for their aid and comfort in times of great travail.

This work was supported by the Nuclear Science Division of the U. S. Department of Energy under contract No. W-7405-ENG-48.

Appendix A. RAMA Helium-Jet Additional Information

The helium-jet technique has been discussed extensively in Section III in terms of what techniques have been found to work well on RAMA. In this appendix, a few additional tips will be given on the "black magic" necessary for successful transport of radioactivity.

To maintain high levels of cluster formation, high beam currents are necessary. With heavy ion beams this creates a formidable problem because of excessive energy losses in the entrance and exit foils. This problem was overcome by using cold nitrogen gas as a window coolant. The nitrogen flow must be directed on the center of the foil to insure that the foils will not overheat when the beam is trebled, the nominal increase over uncooled windows. Cooling the foils has a secondary benefit; it reduces the ethylene glycol concentration which effectively increases the cluster size. The condensation of ethylene glycol on all of the target box surfaces often causes additional ethylene glycol to be released into the system when the target box warms. A careful monitoring of the gas temperature insures that this problem does not arise with great frequency. This condensation of ethylene glycol occurs on all interior surfaces, and thus makes conversion to another additive difficult on a short timescale. This contamination problem is especially important when an attempt is made to use sodium chloride aerosols. The sodium chloride crystals mix with ethylene glycol droplets which may clog the capillary system. Acetone will flush the ethylene glycol from the capillary tube, but water is necessary to dissolve any salt deposits.

It is imperative to monitor not only the target box temperatures, but also the operating conditions (vapor pressure, etc.) for any additive. The right set of conditions for one element may be totally different for another element. The target-projectile combination must also be considered as regards target melting point and projectile energy loss in traversing various target box components. The changing energy losses do not allow for easy quantization of the conditions necessary for the formation of clusters, even though a minimum quantity of projectile energy loss in the helium is necessary for efficient transport.

Transport of products exhibiting charged particle decays are monitored with an annular counter which concentrically observes the skimmer. Other pure β-γ emitters are monitored by observing spot sizes on an interceptor foil. This monitoring becomes especially important for very low count-rate experiments.

Appendix B. RAMA Ion-Source-Additional Information

Some properties of the early Sidenius hollow-cathode ion source used in the RAMA system were discussed in Section III. Since many particular nuances of common ion sourcery have not been explained nor have they been promulgated in regards to the RAMA system, further comments will be directed toward the new shortened version of the ion source since the old system is no longer in use.

Initially the problem of ion source temperature will be addressed. In first order the operating temperature is controlled by the construction material of the surroundings and the filament material. The latter choice is important to control electron emission. Use of molybdenum cathode tubes with copper cathode contacts gives a cold ion source (~1300^{o}C internal temperature). A stable plasma at this low temperature is possible only with 0.50 mm tungsten filaments. Electron emission from larger diameter tungsten filaments becomes comparable only at elevated temperatures. One method of achieving higher temperatures is by using larger filaments operated at higher powers. A second method for raising the operating temperature is by changing the cathode tubes and contacts to tantalum and steel or stainless steel, respectively. Changes to tungsten and graphite ion source pieces should make it possible to further increase the operating temperature.

A common problem with ion source operation is improper assembly. It is imperative that the ion source be cleaned (preferably sand-blasted on occasion) thoroughly, especially evaporated metals (e.g., molybdenum from the outer cathode tube to the anode sleeve (see

Fig. 3-13)). Such rigorous cleaning is necessary to reduce incidences of arc-shorting characterized by the arc power being dissipated by the series glow-coils. The 4.5-6 turns of the filament must be kept cylindrically symmetric to avoid filament shorts. Some compression on the filament is necessary to insure good electrical contact. The boron nitride anode cap insulator must fit tightly without cracking to extend arc lifetimes. This is especially important because boron nitride is isoelectronic to carbon and heating for extended periods to temperatures in excess of 2000°C causes a slow transition to a conducting form of boron nitride, shorting the arc. It is hoped that converting to magnesium oxide insulators will eleminate this problem.

Typical operating conditions for the ion source are filament powers of 300±40 VA and arc powers of 400±50 Watts where the latter is characterized by an arc potential of ~230 volts. For a given arc support gas flow, the arc current may be increased by incresing the filament power. If the filament current is too high, however, the induced solenoidal magnetic field reduces the ion current output. Initial heating of the ion source must be slow to avoid filament breakage from thermal shock. A typical warmup time of 15 m achieves the internal operating temperature of ~2200°C with very stable plasma conditions. These conditions are generally sufficient to ionize many of the elements as noted in Figure B. It should be noted that even though generally a stable arc voltage and current indicate a stable plasma, this is not always the case. These plasma instabilities manifest themselves as oscillations in the extraction voltage

(~50-100 Volts out of 18 kV) and may be cured by a small increase in either the filament power or feed gas flow.

Calibration of RAMA and monitoring of the plasma conditions is accomplished with the channeltron electron multiplier (CEM) mentioned in Section III. Since the CEM is designed for rates varying from 100 Hz to 50 KHz, large beam currents (~1μA) easily saturate the CEM. Beam levels measured at known high current masses (16,18,28) should be ignored on a relative basis and probably should be avoided entirely. Light mass calibrations are most easily accomplished at masses 20 ($^{20}Ne^{+}$ and $^{40}Ar^{+2}$) and mass 40 ($^{40}Ar^{+}$) while the large number of tin isotopes (see Fig. 3-15) provide convenient medium-heavy mass calibrants. The tin is introduced as the non-volatile liquid tetraethyl tin (BP = 181°C) via the arc support gas. Tetraethyl tin is commercially available from Alpha Ventron Corp. or may be easily synthesized by the following reaction sequence:

$$C_2H_5Br + Mg \xrightarrow{\text{ether}} C_2H_5MgBr \qquad \text{(B-1)}$$

$$SnCl_4\,(\text{Anhydrous}) + 4\ C_2H_5MgBr \xrightarrow{\text{ether}} Sn(C_2H_5)_4. \qquad \text{(B-2)}$$

The use of such low vapor pressure additives provide convenient mass calibrations without changing the plasma conditions.

Figure Captions

Fig. B. List of the first one hundred elements with their melting and boiling points and the type of ion source necessary for efficient throughput.

= Gas or liquid = Cold (50-1000C)

= Warm (1000-1500C) = Hot (1500-1900C)

= Very Hot (1900-2300C) = Special Hot Source only (>2300C)

ELEMENT	Z	MP(C)	BP(C)	TYPE OF ION SOURCE
Hydrogen	1	-259	-252	
Helium	2	-272	-268	
Lithium	3	179	1317	
Beryllium	4	1278	2970	
Boron	5	2300	2550(s)	
Carbon	6	3550	4827	
Nitrogen	7	-210	-196	
Oxygen	8	-218	-183	
Fluorine	9	-220	-188	
Neon	10	-249	-246	
Sodium	11	98	892	
Magnesium	12	651	1107	
Aluminum	13	660	2467	
Silicon	14	1410	2355	
Phosphorus	15	44	280	
Sulphur	16	115	444	
Chlorine	17	-101	-35	
Argon	18	-189	-186	
Potassium	19	64	774	
Calcium	20	846	1487	
Scandium	21	1539	2727	
Titanium	22	1675	3260	
Vanadium	23	1890	3000	
Chromium	24	1890	2482	
Manganese	25	1244	2097	
Iron	26	1535	3000	
Cobalt	27	1495	2900	
Nickel	28	1453	2732	
Copper	29	1083	2595	
Zinc	30	419	907	

Fig. B.

Gallium	31	30	2403	
Germanium	32	937	2830	
Arsenic	33	613(S)	613(S)	
Selenium	34	217	685	
Bromine	35	-7	59	
Krypton	36	-157	-152	
Rubidium	37	39	688	
Strontium	38	769	1384	
Yttrium	39	1495	2927	
Zirconium	40	1852	3578	
Niobium	41	2468	4927	
Molybdenum	42	2610	5560	
Technetium	43	2200	-	
Ruthenium	44	2250	3900	
Rhodium	45	1966	3727	
Palladium	46	1552	2927	
Silver	47	961	2212	
Cadmium	48	321	765	
Indium	49	157	2000	
Tin	50	232	2270	
Antimony	51	630	1380	
Tellurium	52	450	990	
Iodine	53	114	184	
Xenon	54	-112	-107	
Cesium	55	29	690	
Barium	56	725	1140	
Lanthanum	57	920	3469	
Cerium	58	795	3468	
Praseodymium	59	935	3127	
Neodymium	60	1024	3027	
Promethium	61	1035	2730	
Samarium	62	1072	1900	
Europium	63	826	1439	
Gadolinium	64	1312	3000	
Terbium	65	1356	2800	
Dysprosium	66	1407	2600	
Holmium	67	1461	2600	
Erbium	68	1497	2900	

Fig. B

Thulium	69	1545	1727	
Ytterbium	70	824	1427	
Lutetium	71	1652	3327	
Hafnium	72	2150	5400	
Tantalum	73	2996	5425	
Tungsten	74	3410	5927	
Rhenium	75	3180	5627	
Osmium	76	3000	5000	
Iridium	77	2410	4527	
Platinum	78	1769	3827	
Gold	79	1063	2966	
Mercury	80	-39	357	
Thallium	81	304	1457	
Lead	82	328	1744	
Bismuth	83	271	1560	
Polonium	84	254	962	
Astatine	85	-	-	
Radon	86	-71	-72	
Francium	87	-	-	
Radium	88	700	<1700	
Actinium	89	1050	3200	
Thorium	90	1700	4000	
Protactinium	91	1230	-	
Uranium	92	1132	3818	
Neptunium	93	640	-	
Plutonium	94	640	3235	
Americium	95	>850	-	
Curium	96	-	-	
Berkelium	97	-	-	
Californium	98	-	-	
Einsteinium	99	-	-	
Fermium	100	-	-	

Fig. B.

Appendix C. Sample RAMA Calculations

In this appendix, a series of sample calculations are given. No beam transport equations are illustrated because they are adequately covered in many standard texts (see, for instance, (He 74)).

Wien Filter

As a charged particle passes through the Wien filter, it experiences a net force F such that

$$F = \frac{mv^2}{R} = q\vec{v} \times \vec{B} + q\vec{\mathcal{E}}, \qquad \text{(C-1)}$$

and since the magnetic force and the electric force oppose one another, Equation (C-1) may be rewritten as

$$\frac{1}{R} = \frac{qvB - q\mathcal{E}}{mv^2} \qquad \text{(C-2)}$$

where B is the magnetic field, $\mathcal{E}$ is the electric field, v is the velocity of the particle with charge q and mass m, and R is the radius of curvature for the emerging particle. Expressing R in terms of the length of the Wien filter and the angle of divergence θ gives

$$\frac{1}{R} = \frac{\sin\theta}{L} \qquad \text{(C-3)}$$

which when substituted into equation (C-2) along with the energy E of the particle gives

$$\frac{\sin \theta}{L} = \frac{vB-\varepsilon}{2E} \qquad \text{(C-4)}$$

or

$$\varepsilon = vB - \frac{2E \sin \theta}{L} \quad . \qquad \text{(C-5)}$$

Under normal operating conditions $\theta = 0^{\circ}$ and Equation (C-5) reduces to

$$\varepsilon = vB = \sqrt{\frac{2E}{m}}\, B, \qquad \text{(C-6)}$$

the form quoted in Section III.

Scaling of optics devices with mass and energy

The electrostatic quadrupole triplet and the vertical deflection plates operate mass independently while the magnetic elements scale as

$$\sqrt{\frac{m_1}{m_{cal}}} \quad ,$$

for example the dipole magnet field for mass 40 scales from the mass 20 calibration numbers as

$$\nu_{40} = \nu_{20} \sqrt{\frac{40}{20}} = \nu_{20}\sqrt{2} \ \text{MHz} \qquad \text{(C-7)}$$

where ν is the NMR frequency in MHz which is related to the magnetic field by the constant 234.875 gauss/MHz (only for a hydrogen water probe). As mentioned in Section III, the electrostatic elements scale

linearly with energy E_2/E_1 and the magnetic elements scale as $(E_2/E_1)^{1/2}$.

Calculation of the resolution

The resolution of the system may be determined by measuring the width of a mass peak on the focal plane. It is given by the relation

$$\text{Res} = \frac{D}{2w} \tag{C-8}$$

where D is the measured dispersion of 1.64 m.

Calculation of the distance between two masses

The distance (ΔS) between two adjacent masses is given by

$$\Delta S = \frac{\Delta\nu}{\bar{\nu}} \tag{C-9}$$

where $\bar{\nu} = 1/2(\nu_m + \nu_{m\pm1})$ and $\Delta\nu = |\nu_m - \nu_{m\pm1}|$. The dispersion was originally determined by measuring the frequency difference $\Delta\nu$ for a mass m at two points on the RAMA focal plane separated by a known distance ΔS.

Appendix D. Error Analysis

Two standard error analysis methods have been developed to exhibit the goodness of a least squares polynomial fit, the χ^2 - and the F- tests (Be 69b). The χ^2 test consists of calculating χ^2 from the definition

$$\chi^2 = \sum \left(\frac{1}{\sigma_i^2} \left[y_i - y(x_i) \right]^2 \right) \qquad \text{(D-1)}$$

where the $y(x_i)$ are the calculated values and the y_i are the measured values. The σ_i^2 are the variances for each point considered in the fit. Multiplying by $\frac{1}{N}$ gives the normalized χ^2 per degree of freedom. The normalized χ^2 would approach one for a perfect fit. This situation arises in the quadratic fit to the mass 20 isospin quintet data.

The χ^2 test is somewhat ambiguous unless the form of the parent function is known because the statistic χ^2 measures not only the discrepancy between the estimated function and the parent function, but also the deviations between the data and the parent function simultaneously. One such ambiguity may be seen in equation (D-1) by examining the case where the data points coincide exactly with the calculated function. The numerator is so small that reduction of the variance (or standard deviations) has little or effect on the χ^2 value. The mass 24 isospin quintet data presents such a case. To check for the goodness of fit, the F-test is employed.

The mathematical rigors of the F-test are given by Bevington (Be 69b) and will not be detailed here. The form of the F-test of interest here is the testing of an additional term. If we obtain two χ^2 distributions for (n) and (n+1) terms, then

$$F_x = \frac{\Delta\chi^2}{\chi^2} \qquad \text{(D-2)}$$

represents a measure of how much the additional term has improved the value of the reduced chi-square. F_x should be small if the fit has not been improved significantly by adding the extra term. In the case of the mass 24 data, addition of the cT_z^2 term gives a large F_x value while addition of either the dT_z^3 or eT_z^4 terms gives a very small F_x value (if we assume a value for the mass of ^{24}Si).

(An 66) J. B. Anderson, R. P. Andres, and J. B. Fenn, Advan. Chem. Phys. 10, 275 (1966).

(Ad 69) E. G. Adelberger, A. B. McDonald, and C. A. Barnes, Nucl. Phys. A124, 49 (1969).

(Ay 74) J. Äystö, P. Puumalainen, and K. Valli, Nucl. Instr. Meth. 115, 65 (1974).

(Ba 66) A. P. Banford, in The Transport of Charged Particle Beams, E. & F. N. Spon, Ltd. (1966) p. 1.

(Bl 66) R. J. Blin-Stoyle and S. C. K. Nair, Adv. in Physics 15, 493 (1966).

(Bl 67) R. Bloch, R. E. Pixley, and P. Truöl, Phys. Lett. 25B, 215 (1967).

(Bo 68a) D. D. Bogdanov, I. Bacho, V. A. Karnaukhov, and L. A. Petrov, Sov. J. Nucl. Phys. 6, 650 (1968).

(Bo 68b) D. D. Bogdanov, I. Bacho, V. A. Karnaukhov, and L. A. Petrov, Sov. J. Nucl, Phys. 6, 807 (1968).

(Be 69a) M. A. B. Bég, J. Bernstein, and A. Sirlin, Phys. Rev. Lett. 23, 270 (1969).

(Be 69b) P. R. Bevington, in Data Reduction and Error Analysis for the Physical Sciences, McGraw Hill (1969) p. 187.

(Bl 69) R. J. Blin-Stoyle, in *Isospin in Nuclear Physics*, *edited by* D. H. Wilkinson, North-Holland (1969) p. 115.

(Bl 75) R. J. Blin-Stoyle, Nucl. Phys A254, 353 (1975).

(Ba 76) K. Bächmann, V. Matschoß, J. Rudolf, A. Steffen, and S. Tsalas, Nucl. Instr. Meth. 139, 343 (1976).

(Bl 76) M. Blann, OVERLAID ALICE, A Statistical Model Computer Code Including Fission and Preequlibrium Models. U. S. Energy Research and Development Administration Report No. CDO-3494-29, 1976 (unpublished).

(Be 79) W. Benenson and E. Kashy, to be published in Rev. Mod. Physics, MSUCL-278 (1979).

(Ch 61) J. D. Childress, Phys. Rev. 123, 1729 (1961).

(Do 72) C. G. Dols, in 4th International Conference on Magnet Technology, Y. Winterbottom, editor, Brookhaven National Laboratory, Upton, N. Y. Sept. 19-22, 1972, p. 791.

(Da 73) H. Dautet, S. Gujrathi, W. J. Wiesehahn, J. M. D'Auria, and B. D. Pate, Nucl. Instr. Meth. 107, 49 (1973).

(De 74) A. de Shalit and H. Feshbach, in Theoretical Physics, John Wiley and Sons, (1974) Vol. 1. p. 853.

(De 79) C. Detraz, D. Guillemand, G. Huber, R. Klapisch, M. Langevin, F. Naulin, C. Thibault, L. C. Carraz, and F. Touchard, Phys. Rev. C19, 164 (1979).

(Es 70) J. E. Esterl, J. C. Hardy, R. G. Sextro, and J. Cerny, Phys. Lett. 33B, 287 (1970).

(Es 71) J. E. Esterl, Lawrence Berkeley Laboratory Report UCLRL-20480, Ph.D. Thesis, unpublished (1971).

(En 73) P. M. Endt and C. Van der Leun, Nucl. Phys. A214, 108 (1973).

(Ge 64) M. Gell-Mann, in The Eightfold Ways, edited by M. Gell-Mann and Y. Ne'eman, W. A. Benjamin (1964) p. 172.

(Go 64) T. S. Goulding, D. A. Landis, J. Cerny, and R. H. Pehl, Nucl. Instr. Meth. 31, 1 (1964).

(Go 72) R. A. Gough, R. G. Sextro, and J. Cerny, Nuclear Chemistry Division Annual Report for 1972, LBL-1666, p. 361 (unpublished).

(Ga 75) H. Gauvin, Y. LeBayec, J. Livet, and J. L. Reyss, Ann. Phys. 9, 241 (1975).

(Ha 71) J. C. Hardy, J. E. Esterl, R. G. Sextro, and Joseph Cerny, Phys. Rev. C3, 700 (1971).

(Ha 73) HAVAR is a trade name for an alloy consisting primarily of Co (42.5%), Ni (13.0%), Cr (20.0%), and Fe (17.9%), with a density of 8.3 g/cm^3, and manufactured by the Metals Division of the Hamilton Watch Co., Lancaster, Pa.

(Ha 74) J. C. Hardy, in Nuclear Spectroscopy and Reactions, edited by J. Cerny, Academic Press (1974) Part C, p. 417.

(He 74) D. L. Hendrie, in Nuclear Spectroscopy and Reactions, edited by J. Cerny, Academic Press (1974) Part A, p. 365.

(Ha 75) J. C. Hardy and I. S. Towner, Nucl. Phys. A254, 221 (1975).

(Ha 77a) E. Hagberg, P. G. Hansen, J. C. Hardy, P. Hornshoj, B. Jonsson, S. Mattson, and P. Tidemand-Peterson, Nucl. Phys. A293, 1 (1977).

(Ha 77b) E. Hagberg, P. G. Hansen, J. C. Hardy, A. Huck, B. Jonson, S. Mattson, H. L. Ravn, P. Tidemand-Peterson, and G. Walter, Phys. Rev. Lett. 39, 792 (1977).

(Ha 77c) J. C. Hardy, Proc. Brookhaven (1977), BNL 50847, p. 309.

(Ha 79) P. G. Hansen, to be published in Ann. Rev. of Nucl. and Part. Sci., CERN EP/79-11 (1979).

(Ho 79) J. Honkanen, M. Kortelahti, J. Äystö, K. Eskola and A. Hautojärvi, to be published in Physics Scripta (1979).

(Ja 69) J. Jänecke, in Isospin in Nuclear Physics, edited by D. H. Wilkinson, North-Holland (1969) p. 297.

(Ja 70) W. Jaus and G. Rasche, Nucl. Phys. A143, 202 (1970).

(Jo 71) H. Jungclas, R. D. Macfarlane, and Y. Fares, Phys. Rev. Lett 27, 556 (1971).

(Ko 65) E. J. Konopinski and M. E. Rose, in Alpha Beta and Gamma Ray Spectroscopy, edited by K. Siegbahn, North-Holland (1965) p. 1327.

(Ku 67) H. M. Kuan, D. W. Heikkinen, K. A. Snover, F. Riess, and S. S. Hanna, Phys. Lett. 25B, 217 (1967).

(Ka 74) V. A. Karnaukhov, D. D. Bogdanov, A. V. Demyanov, G. I. Koval, and L. A. Petrov, Nucl. Instr. Meth. 120, 69 (1974).

(Ko 74) K. L. Kosanke, W. C. McHarris, and R. A. Warner, Nucl. Instr. Meth. 115, 151 (1974).

(Ka 75) E. Kashy, W. Benenson, D. Mueller, R. G. H. Robertson, and D. R. Goosman, Phys. Rev. C11, 1959 (1975).

(Ki 75) R. Kirchner and E. Roeckl, Nucl. Instr. Meth. 131, 371 (1975).

(Ki 76a) R. Kirchner and E. Roeckl, Nucl. Instr. Meth. 133, 187 (1976).

(Ki 76b) R. Kirchner and E. Roeckl, Nucl. Instr. Meth. 139, 291 (1976).

(Ki 77) R. Kirchner, O. Klepper, G. Nyman, W. Reisdorf, E. Roeckl, G. Schardt, N. Kaffrell, P. Peuser, and K. Schneeweiss, Phys. Lett. 70B, 150 (1977).

(Ke 78) G. J. Kekelis, M. S. Zisman, D. K. Scott, R. Jahn, D. J. Vieira, and Joseph Cerny, Phys. Rev. C17, 1929 (1978).

(La 58) A. M. Lane and R. G. Thomas, Rev. Mod. Phys. 30, 257 (1958).

(Le 60) T. D. Lee and C. N. Yang, Phys. Rev. 119, 1410 (1960).

(La 73) W. A. Lanford and B. H. Wildenthal, Phys. Rev. C7, 668 (1973).

(Ma 64) R. D. Macfarlane and A. T. Siivola, Phys. Rev. Lett. 14, 114 (1964).

(Ma 68) J. B. Marion and F. C. Young, in Nuclear Reaction Analysis-Graphs and Tables, North-Holland (1968) p 327.

(Ma 69a) R. D. Macfarlane, R. A. Gough, N. S. Oakey, and D. F. Torgerson, Nucl. Instr. Meth. 73, 285 (1969).

(Ma 69b) P. Marmier and E. Sheldon, in Physics of Nuclei and Particles, Academic Press (1969) p. 316.

(Mu 76) G. F. Millington, R. M. Hutcheon, J. R. Leslie, and W. McLatchie, Phys. Rev. C13, 879 (1976).

(Mc 78) A. B. McDonald, E. D. Earle, W. McLatchie, H. B. Mak, D. J. Martin, and P. G. Ikossi, Nucl. Phys. A305, 151 (1978).

(Ni 70) J. M. Nitschke, in Proceedings of the International Conference on the Properties of Nuclei Far from the Region of Beta-Stability, Leysin, Switzerland, 1970 (CERN, Geneva, 1970) Vol. 1, p. 153.

(Os 78) J. L. Osborne, E. G. Adelberger, and K. A. Snover, Nucl. Phys. A305, 144 (1978).

(Re 67) E. Regenstreif, in Focusing of Charged Particles, edited by A. Septier, Academic Press (1967) Vol. 1, p. 353.

(Ri 67) F. Riess, W. J. O'Connell, D. W. Heikkinen, H. M. Kuan, and S. S. Hanna, Phys. Rev. Lett. 19, 367 (1967).

(Ra 73) S. Raman and N. B. Gove, Phys. Rev. C7, 1995 (1973).

(Re 67) E. Regenstreif, in Focusing of Charged Particles, edited by A. Septier, Academic

(Ri 67) F. Riess, W. J. O'connell, D. W. Heikkinen, H. M. Kuan, and S. S. Hanna, Phys. Rev. Lett. 19 367 (1967).

(Ra 73) S. Raman and N. B. Gove, Phys. Rev. C7, 1995 (1973).

(Ro 73) R. G. H. Robertson and B. H. Wildenthal, Phys. Rev. C8, 241 (1973).

(Ro 74) M. Roos, Nucl. Phys. B77, 420 (1974).

(Ro 75) R. G. H. Robertson, W. S. Chien, and D. R. Goosman, Phys. Rev. Lett. 34, 33 (1975).

(Ro 76) R. G. H. Robertson, W. Benenson, E. Kashy, and D. Mueller, Phys. Rev. C13, 1018 (1976).

(Ro 77a) E. Roeckl, R. Kirchner, O. Klepper, G. Nyman, and W. Reisdorf, Proc. Brookhaven (1977), BNL 50847, p. 331.

(Ro 77b) R. G. H. Robertson, T. J. Bowles, and S. J. Freedman, Nucl. Instr. Meth. 147, 361 (1977).

(Ro 77c) D. W. O. Rogers, N. Anyass-Weiss, S. P. Dolan, N. A. Jelley and T. K. Alexander, Can. J. Phys. 55, 206 (1977).

(Sc 66) H. S. Schopper, in Weak Interaction in Nuclear Beta-Decay, North-Holland (1966) p. 217.

(Si 69) G. Sidenius, in Proceedings of the First International Conference on Ion Sources, Saclay, France (1969) p. 401.

(Se 73a) R. G. Sextro, R. A. Gough, and J. Cerny, Phys. Rev. C8, 258 (1973).

(Se 73b) R. G. Sextro, Lawrence Berkeley Laboratory Report LBL-2360, Ph.D. Thesis, unpublished (1973).

(St 73) D. F. H. Start, N. A. Jelley, J. Burde, D. A. Hutcheon, W. L. Randolph, B. Y. Underwood, and R. E. Warner, Nucl, Phys. A206 (1973) 207.

(Se 74) R. G. Sextro, R. A. Gough, and Joseph Cerny, Nucl. Phys. A234, 130 (1974).

(Si 74) A. Sirlin, Nucl. Phys. B71, 29 (1974).

(Se 75) All optics calculations were performed using standard beam transport equations contained in the codes BELIN and DESS provided by Frank Selph. BELIN was used for first order calculations while DESS was used for calculating second order aberrations.

(Sc 76) H. Schmeing, et. al, Nucl. Instr. Meth. 139, 335 (1976).

(Sp 77) E. Spejewski, Proc. Brookhaven (1977) BNL 50847, p. 149.

(Si 78) G. Sidenius, Nucl. Instr. Meth. 151, 349 (1978).

(To 73) I. S. Towner and J. C. Hardy, Nucl. Phys. A205, 33 (1973).

(Tr 76a) R. E. Tribble, R. A. Kenefick, and R. L. Spross, Phys. Lett. C13, 50 (1976).

(Tr 76b) R. E. Tribble, J. D. Cossairt and R. A. Kenefick, Phys. Rev. 61B, 353 (1976).

(Tr 77) R. E. Tribble, J. D. Cossairt and R. A. Kenefick, Phys. Lett. C15, 2028 (1977).

(Vi 78) D. J. Vieira, Lawrence Berkeley Laboratory Report LBL-7161, Ph.D. Thesis, unpublished (1978).

(Wi 57) E. P. Wigner, Proceedings of the Robert A. Welch Conferences on Chemical Research, Houston, Texas, November 20-22, 1957, Vol. 1, p. 67.

(Wi 72a) K. Wien, Y. Fares, and R. D. Macfarlane, Nucl. Instr. Meth. 103, 181 (1972).

(Wi 72b) D. H. Wilkinson, Comments Nucl. Part. Phys. 5, 135 (1972).

(Wi 73a) H. G. Wilhelm, H. Jungclas, H. Wollnik, D. F. Snider, R. Brandt, K. H. Lust, Nucl. Instr. Meth. 115, 419 (1973).

(Wi 73b) D. H. Wilkinson, Nucl. Phys. A209, 470 (1973).

(We 74) S. Weinberg, Rev. Mod. Phys. 46, 255 (1974).

(Wi 74) W. J. Wiesehahn, J. M. D'Auria, and J. C. Irwin, Nucl. Instr. Meth. 114, 401 (1974).

(Wi 76) D. H. Wilkinson and D. E. Alburger, Phys. Rev. C13, 2517 (1976).

(Wa 77) A. H. Wapstra and K. Bos, At. Data Nucl. Data Tables 19, 175 (1977).

(Wo 77a) F. K. Wohn, in Proceedings of the Isotope Separator On-Line Workshop, R. E. Chrien, editor, Brookhaven National Laboratory, Upton, N. Y., Oct. 31-Nov. 1, 1977, BNL 50847, p. 23.

(Wo 77b) H. Wollnik, J. Portstendörfer, R. Robig, and H. G. Wilhelm, Nucl. Instr. Meth. 144, 247 (1977).

(Zi 74) J. P. Zirnheld, Nucl. Instr. Meth 120, 1 (1974).

(Zi 79) J. P. Zirnheld, L. Schutz, and F. K. Wohn, Nucl. Instr. and Meth. 158, 409 (1979).